Acta Materialia 293 (2025) 121124

Contents lists available at ScienceDirect

Acta Materialia

journal homepage: www.elsevier.com/locate/actamat

Non-Equilibrium Microstructures in Iron-Carbon Thin Films: Co-Evolution of Carbon Clusters and Ferrite Nanograins

J. Arlt [a,*], T. Meyer [a], M. Roscher [a], T. Brede [a], C. Borchers [a], T.M. Schwarz [b,c], P. Stender [b], A. Pundt [d], C.A. Volkert [a]

[a] University of Goettingen, Institute of Materials Physics, D-37077 Göttingen, Germany
[b] University of Stuttgart, Institute for Materials Science, Chair of Materials Physics, D-70569 Stuttgart Germany
[c] now at Max Planck Institute for Sustainable Materials GmbH, Department Microstructure Physics and Alloy Design, D-40237, Germany
[d] Karlsruhe Institute of Technology (KIT), Institute for Applied Materials (IAM-WK), D-76131 Karlsruhe, Germany

ARTICLE INFO

Keywords:
Atom probe tomography (APT)
Thin films
Metastable phases
Nanostructured metals
Carbon-supersaturated ferrite

ABSTRACT

This study investigates how carbon influences the microstructure formation in Fe-C thin films produced by room-temperature sputter deposition. Using 4D-scanning transmission electron microscopy and atom probe tomography, we examined films with varying carbon concentrations (1.3 to 17.1 at.% C). The results show that low-carbon films form crystalline ferrite microstructures, while high-carbon films remain amorphous. At intermediate carbon concentrations, a unique two-step process occurs: small ferrite seeds form in the amorphous film, grow to a critical size, and then undergo a decomposition process that creates nanometer-scale carbon-rich clusters within a carbon-depleted matrix. These clusters contain sub-nm thick nanofaceted regions of higher enrichment, with concentrations typical of transitional carbides, supporting the emerging view that binary iron carbides evolve through a series of transient states. The clusters co-evolve with ferrite nanograins, likely mediated by the Gibbs adsorption effect, linking nanoscale carbon heterogeneities to structural development. The resulting nanostructured films demonstrate remarkable hardness, comparable to advanced nanostructured steels. This study sheds light on how microstructures form in carbon-supersaturated Fe-C systems and may inspire new methods for creating efficient nanomaterials.

1. Introduction

Nanoscale non-equilibrium microstructures are a promising direction for developing novel functional materials [1–3]. In iron-carbon-based nanomaterials, carbon plays a pivotal and multifaceted role. In Fe-C alloys subjected to severe plastic deformation (SPD) [4], carbon segregation stabilizes the grain boundaries introduced during processing [5,6], enabling the formation of (sub)grain sizes as small as a few tens of nanometers [6–8]. In quenching and partitioning (Q&P) processing [9,10], the redistribution of carbon is leveraged to tailor the alloy microstructure and phase composition. This has led to the development of novel steel classes such as nanostructured dual-phase steels [11,12] and nanoprecipitate-rich maraging steels [13,14]. These examples highlight the importance of understanding the intricate interactions between carbon and the iron matrix, including the defect structure, in the design and synthesis of Fe-C-based nanomaterials.

A key aspect of these interactions is the ordering of carbon within the bcc iron lattice and its competition with segregation to defects. In bcc iron, carbon occupies octahedrally coordinated interstitial lattice sites. When the carbon concentration exceeds 0.8 at.% C, it becomes energetically favorable for the carbon atoms to order onto one of the three invariant octahedral sublattices [15,16]. This phenomenon, known as Zener ordering [17], is responsible for the tetragonal distortion observed in high-carbon martensite [18]. Further ordering in a superstructure known as α''-$Fe_{16}C_2$, where specific interstitial sites within one sublattice are occupied, lowers the free energy even more [19–21]. CALPHAD modeling by Naraghi et al. [21] predicts a spinodal decomposition regime between 0.8 and 11 at.% C, where supersaturated[1] Fe-C decomposes into carbon-rich body centered tetragonal (bct) α''- $Fe_{16}C_2$ clusters and a carbon-lean bcc matrix. These theoretical predictions align with experimental observations of finely spaced concentration modulations (1–5 nm) in early-aged martensites [19,23–26]

* Corresponding author at: Friedrich-Hund-Platz 1, D-37077 Göttingen, Germany.
E-mail address: jarlt@gwdg.de (J. Arlt).

[1] The maximum solubility of C in α-Fe at room temperature is less than 0.01 at.% C [22]

https://doi.org/10.1016/j.actamat.2025.121124
Received 9 December 2024; Received in revised form 10 April 2025; Accepted 6 May 2025
Available online 7 May 2025

and the detection of carbon clusters with approximately 11 at.% C, matching the nominal composition of α''-$Fe_{16}C_2$, as common tempering products in various Fe-C-X alloys [26–29].

Defect segregation appears to compete with these ordering processes. Zhang et al. [16] used a self-consistent defect-chemistry approach to compare the chemical potential of carbon in disordered and ordered martensite with that of carbon segregated to extended defects. They found that at concentrations below about 2.6 at.% C, extended defects offer the lowest chemical potential. When sufficient defect sites are available, virtually all carbon atoms become trapped and the formation of α''-$Fe_{16}C_2$ clusters through spinodal decomposition is suppressed. This site energy landscape picture is supported by atom probe tomography (APT) studies, which show predominantly defect segregation (to dislocations and grain boundaries) at carbon concentrations below 1.1 at.% C [29–32]. Whether mediated by defects or driven by spinodal decomposition, the breakdown of supersaturated Fe-C solid solutions holds potential for self-assembled nanostructure formation, especially at high supersaturation levels, where strong demixing on the smallest length scales is anticipated. However, experimental studies focused on this concentration regime are scarce.

Sputter-deposited thin films provide an ideal platform for investigating decomposition-induced microstructure formation in high-carbon Fe-C systems. These films can be produced with a broad range of compositions, reaching up to 72 at.% C [33–35], and are known to form non-equilibrium phases, such as supersaturated ferrite [33,36] and amorphous nanocomposites [37]. Films with carbon contents above 20 at.% C form predominantly amorphous microstructures [34,37–40], while for films with less than 20 at.% C either columnar crystalline (α-Fe, ferrite) [33,35,36] or homogeneous amorphous Fe-C microstructures [36,41] have been reported. Notably, a large overlap is observed: the highest carbon-concentrated film that remained crystalline contained 17(2) at.% C, while the lowest predominantly amorphous film contained 8.3(8) at.% C [36]. This suggests that, beyond composition, deposition conditions such as substrate temperature and background pressure also determine whether films crystallize or remain amorphous. Interestingly, carbides are rarely observed in Fe-C films, even at high concentrations, with the exception of one case involving films containing 30 to 36 at.% C [38]. The relationship between the different Fe-C film microstructures and their corresponding carbon distribution has been explored in only a few studies [36,41]. A uniform carbon distribution was reported in an atom probe tomography (APT) analysis of an amorphous film with 14 at.% C [41]. Similarly, a study using scanning transmission electron microscopy (STEM) combined with electron energy loss spectroscopy (EELS) found a uniform distribution in a crystalline film containing 11(3) at.% C [36]. However, the STEM-EELS study may have missed nanoscale inhomogeneities, as resolving fine 3D structures is challenging when their size is smaller than the specimen thickness.

In this study, we employ (S)TEM and APT to investigate the microstructure and carbon distribution of ion-sputtered iron-carbon films with carbon concentrations ranging from 1.3 to 17.1 at.% C. By combining (S)TEM and APT, we achieve nanoscale resolution of structural and compositional variations, with APT providing superior 3D chemical mapping of carbon and overcoming the limitations of STEM-EELS in detecting fine heterogeneities. Of particular interest is a complex microstructure that emerges at intermediate carbon concentrations: a retained amorphous Fe-C interlayer that transitions into nanostructured columnar ferrite. Our findings show that these ferrite nanocolumns, typically 5–10 nm in width, are closely associated with planar carbon-rich clusters, suggesting an interplay between chemical decomposition and nanograin evolution. We propose that this microstructure is formed in a complex two-step growth process, where carbon distribution and phase separation play key roles.

2. Experimental

2.1. Iron carbon film preparation

Ion-beam sputter deposition with an adjustable composite target was used to produce Fe-C films with different carbon contents. The base target was a purified iron sheet produced at the Max-Plank-Institut für Eisenforschung in Düsseldorf, Germany, containing impurities such as Mn, Cr, or Co in concentrations lower than 10 ppm [42]. By partially covering the iron sheet with graphite foil strips of variable size (99.8 % pure, 0.4 mm thick, Alfa Aesar) of variable size, we could tune the carbon content in the Fe-C films (supplementary materials, **Figure SI 1**). The deposition parameters were as follows: base pressure of (1 – 8) x 10^{-6} Pa, working pressure of (0.8 – 1) x 10^{-2} Pa in an Ar atmosphere, a beam voltage of 600 V, and a beam current of 20 mA. The substrate was not actively heated but reached temperatures between 80 and 120°C during deposition, as checked periodically using a thermocouple.

The substrates for deposition were pieces (1 × 1 cm^2) of 0.525 mm thick B-doped 100-Si wafers, deposited with 30 nm amorphous SiO_2 and a final layer of 140 nm amorphous Si_3N_4.

2.2. Electron probe microanalysis

The carbon content of the Fe-C films was determined using electron probe microanalysis (EPMA) with a JEOL JXA iHP200F at the Geowissenschaftliches Zentrum, Göttingen University. Measurements were conducted at 10 kV accelerating voltage, 20 nA probe current, and a 15 μm beam size, using the Fe-K_α X-ray line (analyzed with a LiF crystal) and the C-K_α line (analyzed with a layered dispersive element, Ni-C, with a 2d spacing of 80 Å). Further methodological details are provided in Supplementary Note S1. EPMA is routinely used to quantify carbon in ferrous alloys [43–46], and its accuracy in this study is demonstrated by its uncalibrated measurement of 25.2(3) at.% C in Fe_3 C from a cohenite standard [47], in excellent agreement with the stoichiometric value. For all Fe-C films, carbon concentrations were subsequently calibrated using the cohenite and high-purity iron standards. Final concentrations, determined from the mean of ten measurements per sample, are listed in Table 1 along with film thicknesses determined via cross-sectional TEM.

2.3. Nanoindentation testing

To assess the mechanical properties of the mid-carbon films, we measured the hardness of the 8 at.% C film using a Nanoindenter Agilent G200. We performed a total of 27 indents across three distinct locations on the sample, with each location featuring 9 indents. The measurements were conducted using a Berkovich diamond XP tip and the continuous stiffness measurement (CSM) method [48], with a maximum indentation depth of 200 nm. The tip oscillated at a frequency of 45 Hz with an amplitude of 2 nm. Hardness values were calculated using the Oliver-Pharr method [48,49]. In brief, the contact stiffness is extracted by analyzing the unloading curve, from which the projected contact area at peak load is determined, and nanoindentation hardness is then calculated as load divided by projected area (expressed in GPa).

Table 1
Carbon concentration (EPMA) and film thickness (TEM) of sputtered Fe-C films.

Film	Carbon concentration [at.% C]	Film thickness [nm]
(1)	1.32(7)	597(30)
(2)	6.6(4)	541(27)
(3)	8.0(3)	364(19)
(4)	10.9(4)	397(20)
(5)	17.1(3)	441(22)

2.4. TEM and APT sample preparation

For TEM and APT sample preparation via focused ion beam (FIB), we either used a FEI Nova NanoLab 600 or a Thermo Fischer Helios G4 UC. The APT specimens were prepared following well established preparation protocols [50]. In brief, through lamella lift out and subsequent annular milling, specimens solely containing the Fe-C film with the film in-plane direction aligned parallel to the APT tip axis were prepared (supplementary material**, Figure SI 9**).

For (S)TEM two different specimen geometries were used. In addition to a standard cross-sectional lamella, we prepared a 4°-tilted plan-view lamella to minimize projection overlaps inherent in cross-sectional imaging of columnar nanograins. This was achieved by cleaving the sample and extracting a cross section from the cleavage plane. By tilting the lamella ~4° relative to the film surface, we created a gradient along the film growth direction, enabling depth-resolved analysis within a single TEM slice (supplementary material**, Figure SI 9**). This setup significantly reduces overlap between adjacent grains, as they are imaged along their long axis, which enables probing of individual nanocolumns (~10 nm in diameter) using 4D-STEM with a beam spot size less than 2 nm. Lamella thicknesses were determined via the log-ratio method using the inelastic mean free path of 133 nm expected for a density of 7.8 g/cm^3 according to Iakoubovskii et al. [51].

2.5. TEM and APT data analysis

For TEM bright and dark field imaging as well as selected area diffraction (SAED), we used a Philips CM12 operated at 120 kV and an image corrected FEI Titan 80-300 ETEM operated at 300 kV. Furthermore, we used the latter instrument to conduct four-dimensional scanning TEM (4D-STEM) and electron energy-loss spectroscopy (EELS) with beam currents of 10 pA and 42 pA as well as convergence semi-angles of 1 mrad and 10 mrad, respectively. The 4D-STEM data was acquired with a custom script [52] using a Gatan UltraScan 1000XP binned by 8 and a camera length of 48 mm leading to a sampling in reciprocal space of 0.136 nm^{-1}/px. The EELS data was collected with a Gatan GIF Quantum 965 ER including a Gatan UltraScan 1000XP camera using a dispersion of 0.5 eV/channel and a collection semi-angle of 23 mrad.

APT was performed using a straight flight path wide-angle atom probe [53] at the Institute for Materials Science Stuttgart. Measurements were conducted in laser mode ($\lambda = 345$ nm, 200 kHz repetition rate, 250 fs pulse width, 25–30 mW laser power). The specimen base temperature was maintained between 60–70 K, with an initial detection rate of 0.1–0.2 ions per 100 pulses, later increased to 0.6 ions per 100 pulses. APT data analysis, including mass spectra evaluation, ion assignment, and volume reconstruction, was performed using the Scito software [54]. Reconstruction parameters, including depth scaling, were optimized based on TEM inputs such as the evaporated volume and initial and final APT tip radii (see Supplementary **Figure SI 10**), alongside the Fe^+ vs. Fe^{++} ions charge state ratio [55]. A representative mass spectrum and the corresponding ion assignment are provided in Supplementary **Figure SI 6**.

To ensure reliable carbon quantification at the nanoscale, we calibrated APT and STEM-EELS measurements using EPMA as macroscopic reference. EELS carbon quantification can be affected by local hydrocarbon contamination due to the electron beam [56], while APT frequently underestimates carbon content due to detection losses from multiple-hit events [57–59] and from post-dissociation of molecular carbon-containing ions [59,60], as well as ambiguities in carbon-associated peaks [61,62]. Our full calibration approach is detailed in Supplementary Note S1, along with an in-depth analysis of the carbon underrepresentation in APT, which we trace primarily to multiple-hit events and delayed evaporation.

3. Results

3.1. Carbon-dependent film microstructure

Representative TEM micrographs of low and high carbon films are compared in Figure 1. The low carbon film (1.32(7) at.% C) consists of columnar grains with an in-plane grain size of about 50–150 nm. The selected area electron diffraction pattern (SAEDP) (Figure 1**b**) is consistent with bcc α-Fe and shows no signs of other phases such as carbides, which is further confirmed by θ–2θ XRD scans (see Supplementary Material, **Figure SI 11**). Contrast variations within the columnar grains (Figure 1**c**), including dark regions or speckles, arise from differences in grain orientation and defects. In contrast, the high carbon film (17.1(3) at.% C) is fully amorphous, as indicated by the homogeneous grey contrast and the diffuse ring pattern in SAEDP (Figure 1**d**), and confirmed by θ–2θ XRD (see supplementary material**, Figure SI 12**).

The intermediate carbon films (6.6(4) to 10.9(4) at.% C) exhibit a complex microstructure (Figure 2). There is a continuous amorphous interlayer directly on the substrate, topped by a columnar crystalline film. The interlayer thickness varies with position and its average thickness increases with the film carbon content (4.8(3) nm for 6.6(4) at.% C, 7.9(2) nm for 8.0(3) at.% C, and 26.1(5) nm for 10.9(4) at.% C). The crystalline layer begins as small seeds, a few 10 nm in diameter, partially embedded in the amorphous interlayer (Figure 2**a** and **e**). These seeds develop into columnar grains that eventually merge into a dense, fully crystalline film. SAEDP of the crystalline part is consistent with bcc α-Fe, without evidence for any second phases (cf. Section 3.2). Dark field imaging (Figure 2**b**) confirms that most of the columns originate in the amorphous interlayer and extend throughout the entire film to the surface, appearing to maintain the crystal orientation of the initial seed (a detailed texture analysis is provided in Section 3.2). The columns increase from a few 10 nm in diameter near the film bottom to 150–200 nm towards the surface. Extended defects, visible as dark lines (red arrows), subdivide these columns into nanograins (subgrains) with similar crystal orientations. Sharply defined Moiré patterns (Figure 2**c**) reveal that these grains are 5 to 10 nm wide and elongated along the film growth direction. These nanograins become noticeable when the seeds reach a certain size, with only minimal amorphous material remaining between them (Figure 2**e,** yellow arrows).

To investigate the carbon distribution at the amorphous/crystalline interface, we employed STEM-EELS. Figure 3 shows the resulting carbon concentration map alongside the corresponding annular dark field (ADF) image. In the ADF image (Figure 3**a**), the amorphous interlayer appears with homogeneous grey contrast, while the ferrite seeds show varying intensities depending on their crystallographic orientation with respect to the electron beam. The carbon map (Figure 3**b**) reveals a distinct partitioning: the primary α-Fe seeds near the interface are carbon-depleted (~4 at.%), while the amorphous interlayer is homogeneously enriched (~12 at.%). Moving upward along the growth direction (white dashed arrow), the seeds show progressively higher carbon content, indicating that the initial compositional contrast fades with continued film growth. One apparently carbon-rich seed (dashed white circle) likely results from projection overlaps in STEM imaging. In three dimensions, the interface forms a hilly topography, with ferrite seeds sitting in valleys and ridges of amorphous material separating them. Given the seed size (a few 10 nm) and the TEM lamella thickness (~100 nm), such topography leads to overlaps between crystalline and amorphous regions in projection. This effect also systematically affects the STEM-EELS measurements: the initial carbon content of the α-Fe seeds is likely overestimated, while that of the amorphous interlayer is underestimated.

3.2. Depth-dependent nanostructure and texture

To enable depth-resolved analysis of the complex microstructure

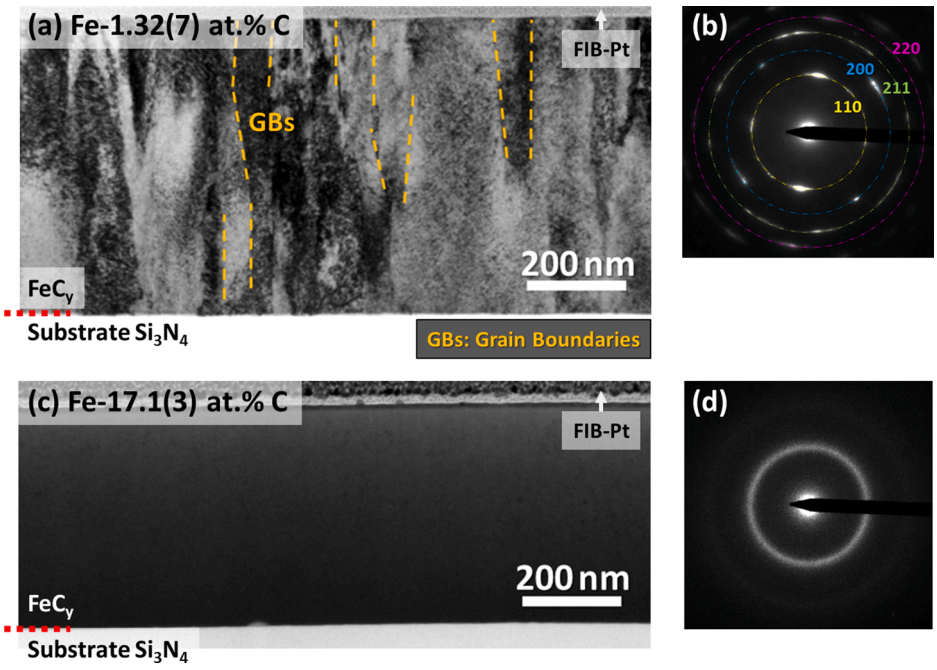

Figure 1. TEM cross-sections and corresponding SAEDP of the Fe-C films with the lowest (Fe-1.32(7) at.% C) and highest (Fe-17.1(3) at.% C) carbon content. The substrate, Fe-C film, and platinum coating (bottom to top) are labeled on the left. **(a, b)** The low-carbon film is fully crystalline with columnar grains (grain boundaries marked in orange). The SAED pattern is consistent with polycrystalline bcc α-Fe (diffraction rings indicated). **(c, d)** The high-carbon film appears fully amorphous, showing uniform contrast and diffuse diffraction rings.

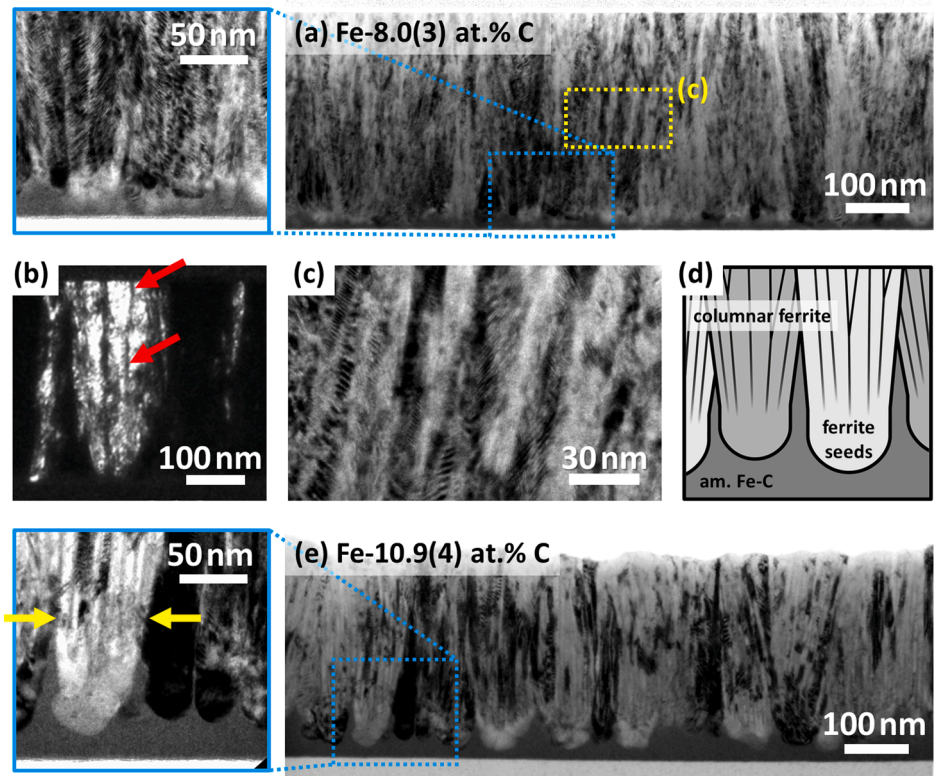

Figure 2. TEM cross-sections of Fe-C films with intermediate carbon content (8.0(3) and 10.9(4) at.% C). (**a, e**) Both films show a two-layer structure: an amorphous Fe-C layer (homogeneous gray contrast) and a columnar crystalline α-Fe layer. The amorphous layer thickens with increasing carbon content. Nanosized subgrains emerge within the columns once the seeds grow beyond a critical size (yellow arrows in e). (**b**) {110} dark field image of the Fe-8.0(3) at.% film highlighting the columnar structure and extended defects (red arrows) subdividing the grains. (**c**) Moiré patterns reveal columnar nanograins with diameters of 5–10 nm. (**d**) Schematic of the layered microstructure with columnar ferrite grains (thick lines) and nanograin substructure (thin lines).

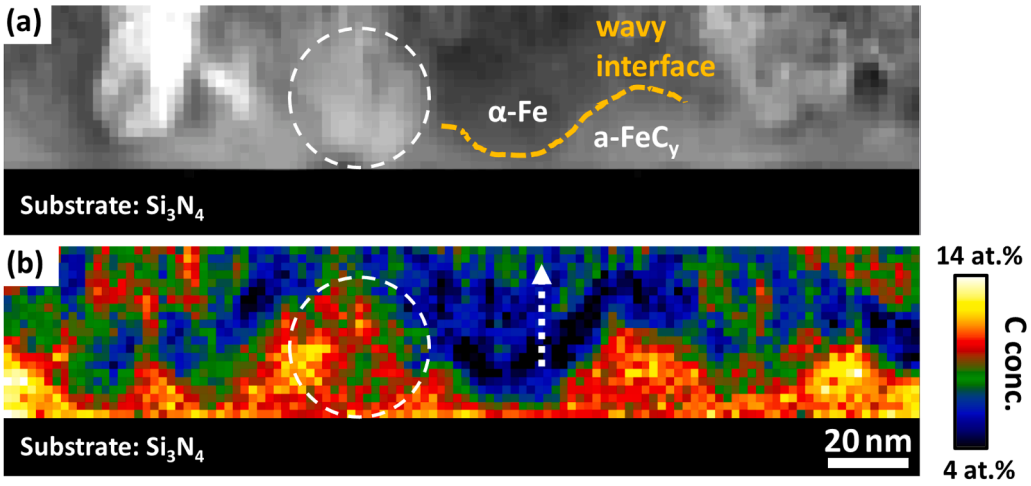

Figure 3. Annular dark field image (a) and STEM-EELS carbon map (b) of the interlayer region in the Fe-8.0(3) at.% C film. (**a**) α-Fe seeds (varying intensity) sit atop the amorphous interlayer (homogeneous intensity), forming a wavy phase boundary (orange dashed line). (**b**) The α-Fe seeds are carbon-depleted α-Fe (~4 at. % C), while the interlayer is uniformly carbon-enriched (~12 at.% C). Moving away from the interface, the seeds' carbon content increases (white dashed arrow). One seed appears enriched (white dashed circle).

while minimizing projection overlaps between columnar nanograins, we employed 4D-STEM on a 4°-tilted plan-view lamella of the 8.0(3) at.% C film (Figure 4). At the left edge (Figure 4**A**), the amorphous Si_3N_4 substrate is visible. Moving rightward, the amorphous Fe-C interlayer with embedded crystallites appears, followed by the dense crystalline α-Fe film (Figure 4**B**), which coarsens toward the surface. Summed diffraction patterns (DPs) confirm this phase identification (Figure 4**a–d**). Notably, no extended amorphous regions or carbides were detected within the crystalline film by 4D-STEM, confirming that the upper part consists of fully crystalline α-Fe columns (cf. Figure 2).

To probe local misorientations between nanograins, we compared DPs from regions spaced ~15nm apart (Figure 4**e** shows a representative example). The colored overlay reveals a small angular offset of 3(1)°, calculated from rotations of individual Bragg reflections such as (110) and (200). Such subtle misorientations, typically on the scale of 10–15 nm, occur regularly throughout the crystalline film. These findings suggest that the film consists of well-aligned nanograins with only slight angular deviations between neighboring grains.

To study the microstructural evolution along the growth direction, we performed 4D-STEM on a cross-section lamella of the Fe–8.0(3) at.% C film (Figure 5). Summed diffraction patterns extracted from rectangular regions reveal a strong {110} out-of-plane (oop) texture near the amorphous/crystalline interface (Figure 5**a**), originating from initially {110}-oriented ferrite seeds (Figure 5**A**, red). This texture gradually fades with increasing film height: residual intensity remains at 80 nm (Figure 5**b**) but nearly vanishes by 160 nm (Figure 5**c**). Alongside this, crystallites with tilted {110} orientations (~40–50° from the oop direction; blue and green in Figure 5**A**) span the full film thickness, intersecting and replacing the initial oop-oriented grains. This observation demonstrates that the texture change is led by these tilted grains replacing the {110}-oriented grains within a few tens of nanometers. This second population likely corresponds to the grains observed in the conventional {110} dark field image (Figure 2**b**).

To resolve the emerging texture, we performed pole figure measurements on the same 8.0(3) at.% C film (for details, see Supplementary Note S2). The resulting orientation distribution function (ODF) reveals a fiber-textured film with two equally strong components: a slightly tilted {111}<uvw> fiber and a {031}<uvw> fiber. Closer inspection of the {111} fiber shows that it varies in orientation between {111}, {322}, and {332}. In addition, a weak (011) [011] component is observed. These findings corroborate the 4D-STEM data: the (011) [011] component corresponds to the initial layer of {110}-oriented crystallites, while the {111} component represents the tilted grains[2]. The {031} component, although not captured in 4D-STEM, is clearly visible in cross-sectional TEM-SAEDP (see supplementary material, **Figure SI 14**).

3.3. Local carbon distribution

We used atom probe tomography to examine the carbon distribution in the Fe–8.0 at.% C film. TEM imaging before and after APT confirmed that the probed volume contained only the columnar ferrite region, excluding the amorphous Fe–C interlayer (supplementary material, **Figure SI 10**). Isoconcentration surfaces extracted from a series of thin slices reveal pronounced carbon clustering on a 5–10 nm scale (Figure 6). The clusters appear plate-like and are nearly parallel in cross-section (Figure 6**c, f**), while plan-view imaging reveals in-plane, ring-like arrangements (Figure 6**d**), suggesting that the clusters decorate the columnar nanograin boundaries (indicated in blue in Figure 6**a**).

The nested character of the clusters complicates a clear delineation of their lateral dimensions. However, based on the isosurface maps, individual clusters are estimated to extend approximately 10–20 nm in the out-of-plane direction (Figure 6**c, f**) and 5–10 nm in the in-plane direction (Figure 6**d**). Concentration profiling reveals that the clusters are approximately 3 nm thick and contain on average 10–12 at.% C, with a matrix concentration of 5.1(1) at.% C (Figure 6**e**).

The cluster surfaces are irregular with modulation on a sub-5 nm scale (Figure 6**f**). Closer inspection using carbon distribution maps reveals that some clusters exhibit faceted surfaces (Figure 7**a**). These faceted regions are a few nanometers in length, sub-nanometer thick, and rich in carbon, with peak concentrations reaching up to 27–31 at.% C (Figure 7**b**). This suggests that some clusters may have already partially transformed into nanofaceted carbides, consistent with the interpretation and terminology proposed by Lu et al. [63].

[2] Grains with {110} planes tilted by approximately 40–50° relative to the film normal (oop direction) are consistent with having {111} planes oriented along the growth direction.

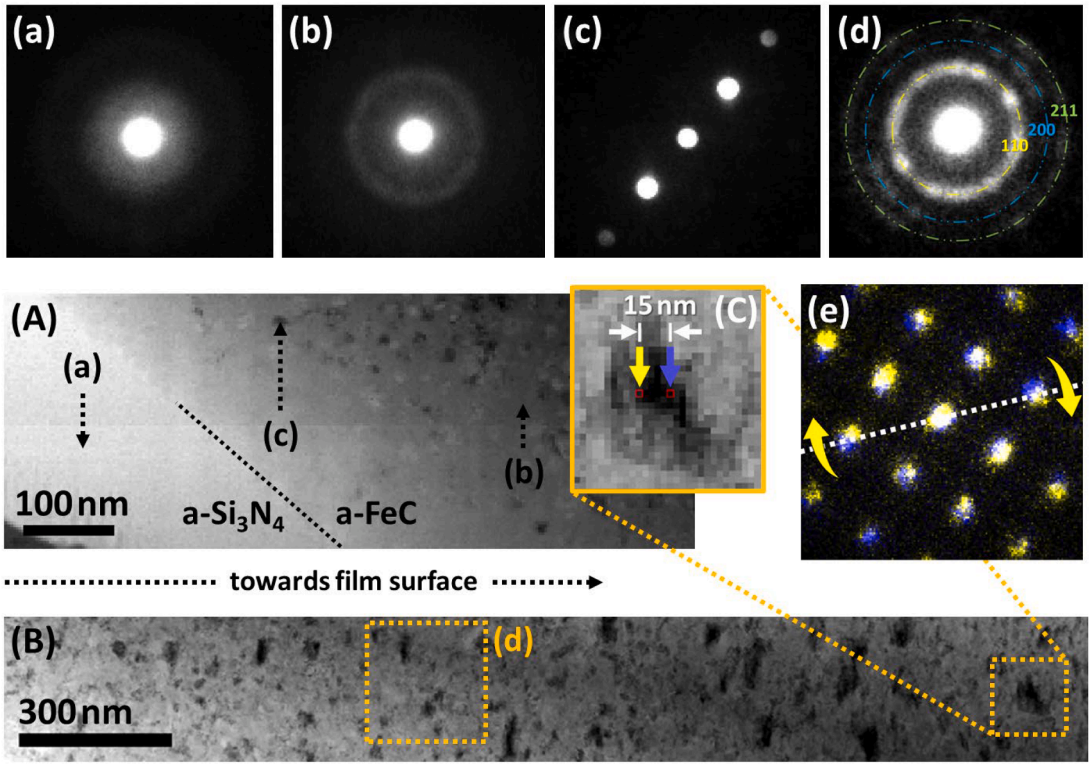

Figure 4. 4D-STEM of the 8.0(3) at.% C film. The plan-view lamella was cut with a 4° inclination relative to the film surface, enabling plan-view imaging from substrate to surface (left to right). (**A, B**) Virtual bright field images at the substrate and mid-height, respectively. (**a–d**) Summed diffraction patterns (DPs) from the marked regions: (a–c), from 6 × 6 nm^2 areas (d), from a 225 × 225 nm^2 area. The DPs show signals from amorphous Si_3N_4 (a), amorphous Fe-C (b), single-crystalline α-Fe (c), and polycrystalline α-Fe (d). (**e**) Colored overlay of two DPs taken ~15 nm apart (marked in C); blue and yellow indicate dominant contributions from the respective regions, white indicates equal contribution. See supplementary material for lamella geometry (**Figure SI 9**).

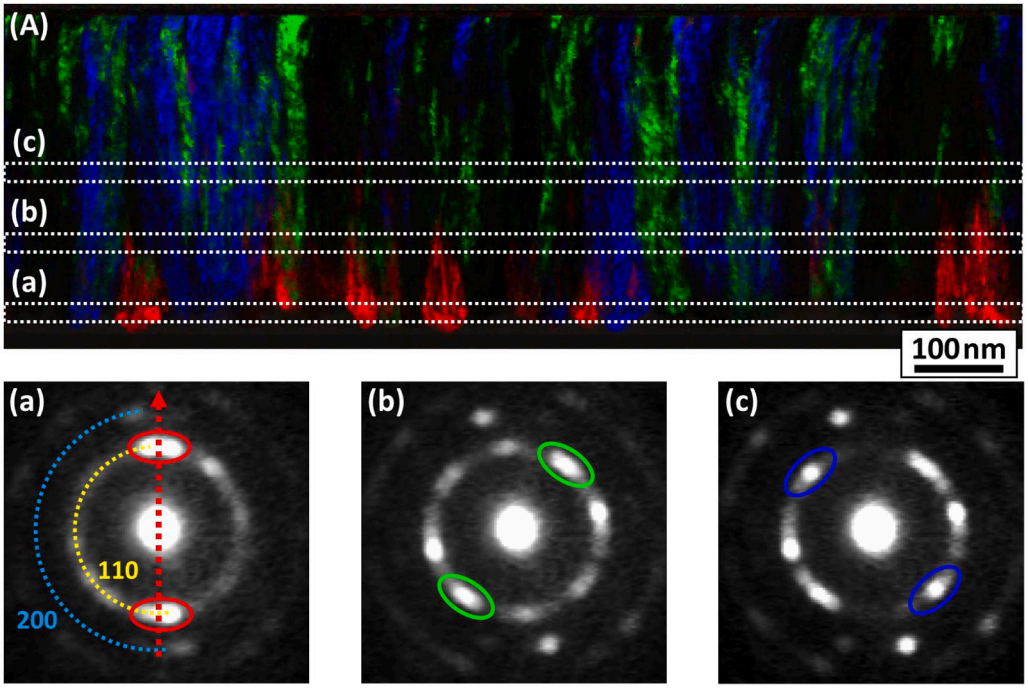

Figure 5. 4D-STEM of the 8.0(3) at.% C film in cross-section. (**a–c**) Summed diffraction patterns (DPs) from rectangular regions (1140 nm × 20 nm each), spaced 80 nm apart starting from the amorphous/crystalline interface. Reciprocal and real space are aligned; the red arrow in (a) indicates the film out-of-plane (oop) direction. An initial {110} oop texture (a) diminishes with increasing film height (b, c). (**A**) Overlay of colored virtual dark field images based on virtual apertures shown in (a–c); red, blue, and green indicate different {110} grain orientations with respect to the film oop direction.

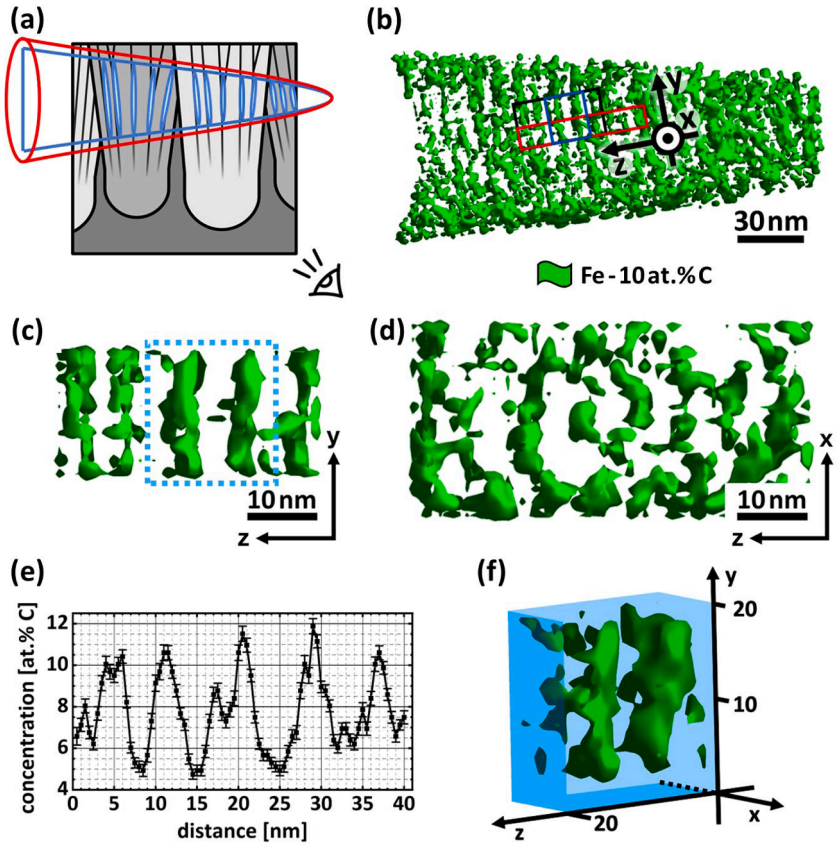

Figure 6. Carbon isoconcentration surfaces from the Fe–8.0 at.% C film, extracted from APT data using 10 nm thin slices. Isosurfaces were generated using 4 × 4 × 4 nm^3 half-overlapping voxels and a 10 at.% C concentration threshold. (**a**) Schematic of the APT tip (red) and slice orientation for (b) (blue) relative to the columnar microstructure. (**b**) Cross-sectional slice through the full dataset; colored boxes and the local coordinate system mark the orientation of the enlarged views in (c, black), (d, red), and (f, blue). (**c, f**) Enlarged cross-sectional views showing plate-like clusters with near-parallel alignment along the growth direction; (f) shows the clusters marked in (c) under a slight tilt; distances are given in nm. (**d**) Plan-view reveals in-plane, ring-like arrangements of clusters. (**e**) Concentration profile across the five clusters in (c), extracted left to right and laterally averaged across the full shown area.

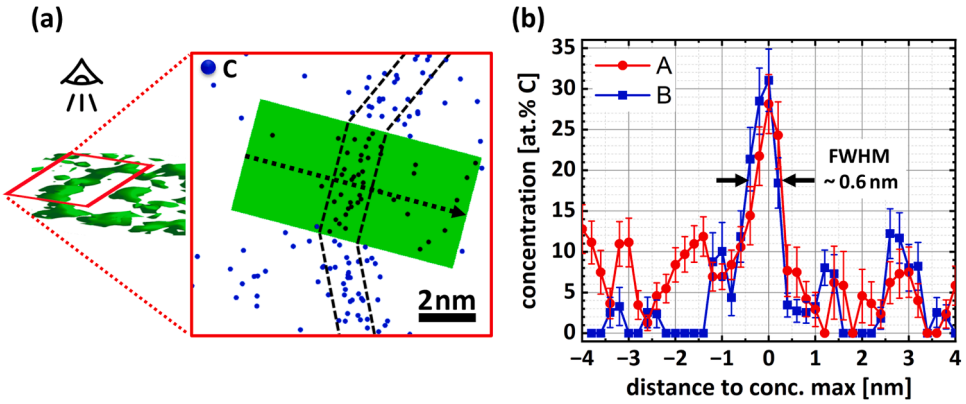

Figure 7. Local carbon distribution along individual clusters. (**a**) Plan-view carbon map of a cluster showing nanofaceting (dashed lines); the isosurfaces to the left illustrate how the carbon maps were extracted but do not correspond to the same cluster. The dashed arrow indicates the profiling direction used to generate profile A shown in (b). (**b**) Concentration profiles across two nanofaceted regions (A and B), taken using a cylindrical probing volume (radius: 1.5 nm, length: 8 nm, resolution: 0.2 nm) and aligned to their concentration maxima. Gaussian fits yield full widths at half maximum (FWHM) of 0.6(2) nm and 0.7(2) nm, respectively.

3.4. Nanoindentation hardness of the mid-carbon films

To assess the mechanical properties of the mid-carbon films, we conducted nanoindentation hardness testing on the 8 at.% C film (Figure 8). The highest nanoindentation hardness, averaging 21(2) GPa, was recorded between 40 and 60 nm in depth. Beyond 60 nm, the hardness gradually decreased, leveling off at 16.8(4) GPa at 200 nm. This indicates that the underlying layered SiN/SiO/Si is softer, with a hardness below approximately 17 GPa, consistent with literature reporting values of 14–15 GPa for amorphous Si_3N_4 [64], and about 10–12 GPa for (100)-Si [65,66] and amorphous SiO_2 [67]. According to literature [68,69], the substrate influence becomes stronger for depths greater than 10% of the film thickness, allowing us to estimate that the film hardness is 21 GPa or larger.

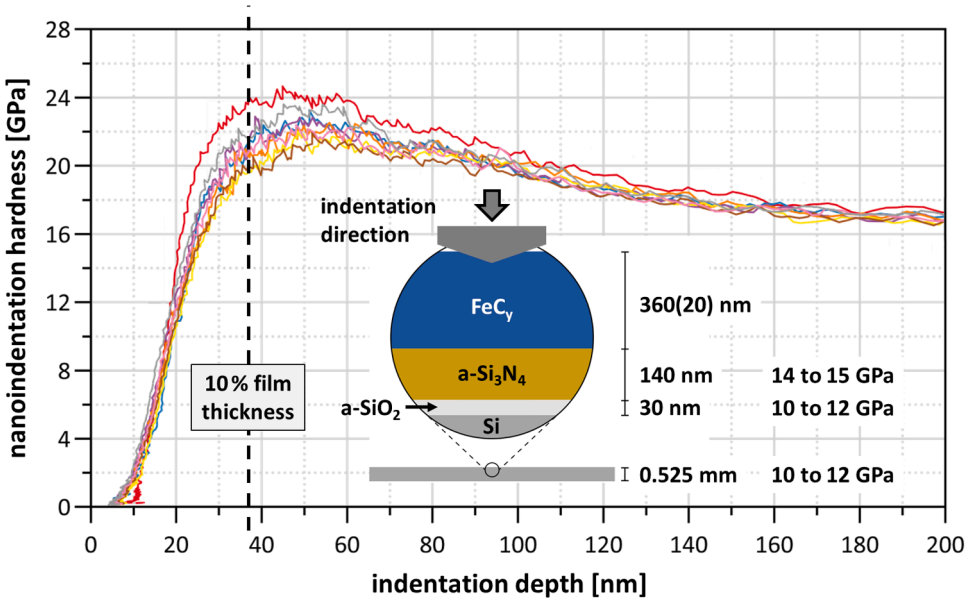

Figure 8. Nanoindentation hardness of the 8 at.% C film as a function of indentation depth. A selection of representative curves is shown to illustrate the overall trend. The hardness peaks on average at 21(2) GPa between 40 and 60 nm, then gradually decreases to 16.8(4) GPa at 200 nm. The peak values at shallow depths reflect the hardness of the Fe-C film, while the decline beyond 60 nm is due to the increasing influence of the softer substrate. The inset shows a sketch of the layered $Si_3N_4/SiO_2/Si$ structure, along with layer thicknesses and hardness values from the literature [64–67].

4. Discussion

In this study, we have observed significant variations in the microstructure of Fe-C films depending on carbon content. Low-carbon (1.3 at.% C) films consist solely of columnar ferrite, while high-carbon (17.3 at.% C) films are fully amorphous. Both microstructures are consistent with literature observations for similar carbon contents. In contrast, the mid-carbon films (6.6 to 10.9 at.% C) develop a complex microstructure. To understand the origins of this microstructure, we first examine the growth mechanism of the mid-carbon films (Section 4.1), then apply these insights to discuss the thermodynamics and growth kinetics of Fe-C thin films across the entire examined carbon concentration range (Section 4.2). Section 4.3 examines the texture evolution of the mid-carbon films. Lastly, in Section 4.4, we explore the structural and mechanical similarities between the mid-carbon films and iron-carbon alloys produced by severe plastic deformation.

4.1. Growth kinetics of the mid-carbon films

The microstructure of the mid-carbon films consists of a bottom layer of ferrite seeds within an amorphous matrix, topped by a fully crystalline film (Figure 2) containing finely dispersed carbon clusters (Figure 6**d**). Given the deposition conditions, amorphous regions or even fully amorphous films are expected. The formation of amorphous metal films during physical vapor deposition (PVD) is well established and was historically the first method used to produce amorphous metals [70]. Metal atoms arriving at the substrate undergo rapid quenching from the vapor into the amorphous solid phase, with estimated cooling rates of $\sim 10^{13}$ K/s [71]. Counterintuitively, this rapid thermal arrest does not result in low-density, poorly stabilized metallic glasses, but rather in highly stable — so-called ultra-stable — glasses [71,72]. This stability is attributed to the high atomic mobility at the growing film surface, allowing each deposited layer to efficiently explore the potential energy landscape and approach a near-equilibrium state [71–74]. As deposition continues, the advancing film surface locks atoms into place, and once buried beyond a few monolayers, they no longer benefit from the high surface mobility.

We propose that the microstructure of the mid-carbon films evolves through a similar scenario, where the advancing film surface governs microstructural development and leaves behind the microstructure observed by TEM and APT. Under this assumption, film height — i.e., distance from the substrate — serves as a proxy for temporal evolution during deposition. In the following sections, we demonstrate that this perspective offers a robust framework for understanding the film's microstructure formation in two distinct growth stages.

4.1.1. Stage I: Formation of primary ferrite seeds

The transition from the amorphous interlayer to the fully columnar crystalline film is initiated by distinct primary ferrite seeds (Figure 2, **a** and **e**). The varying, sometimes nearly spherical shape of these seeds is best explained by assuming their formation both within and at the surface of an amorphously growing film during deposition. The seed-free amorphous layer near the substrate (Figure 2**e**) likely results from an increased carbon content due to carbon-containing adsorbates on the substrate, which are commonly observed even on thoroughly cleaned surfaces [75,76].

Ferrite seeds nucleate and grow into the surrounding amorphous matrix by consuming iron and expelling carbon. Growth toward the substrate slows down and eventually stops when the carbon content in the matrix reaches a certain threshold, as discussed further in Section 4.2. In contrast, growth near the film surface continues due to the ongoing supply of incoming material, which dilutes the carbon concentration in the near-surface regions. Subsurface seeds will eventually reach the film surface if their growth velocity exceeds the film growth rate of 3 nm/min. This assumption is reasonable, as carbon diffusion in amorphous Fe-C is sufficiently fast[3], and crystallization experiments by Fillon et al. [41] report a ferrite / amorphous FeC_y interface velocity of up to 12 nm/min at 250°C. Concurrently, seeds at the surface continue to grow by incorporating incoming iron atoms, while the newly arrived carbon migrates toward nearby amorphous Fe-C regions. However, once

[3] Carbon diffusion in amorphous Fe-C is expected to be faster than in ferrite [41,77,78]. Thus, as a conservative estimate, the diffusion length in ferrite can be used, calculated as $x_d \sim \sqrt{t \cdot D}$ with $D = D_0 \exp[Q/(RT)]$, where $D_0 = 6.2\ 10^{-7}$ m^2/s, $Q = 80$ kJ/mol and $R = 8.31$ J/(K·mol) [79], yielding 7 to 29 nm/min for the temperature range of 80 to 120°C prevailing during deposition.

the seeds reach a critical size, not all incoming carbon can escape — some becomes trapped, buried beneath the subsequent deposited layers. This initiates a fundamental shift in growth behavior, which we refer to as stage II, ultimately leading to the coevolution of carbon clusters (Section 4.1.2) and ferrite nanograins (Section 4.1.4).

4.1.2. Stage II: Carbon cluster formation via surface-layer spinodal decomposition

The forced carbon uptake of surface seeds that have grown beyond a critical size rapidly enriches them in carbon (cf. Figure 3**b**), as the mid-carbon film in question was sputtered with an average composition of 8.0 at.% C. This exceeds the disorder/order transition threshold in bcc Fe-C by a factor of ten [15,16]. Thus, once ferrite seeds begin incorporating carbon, the system strongly favors ordering. The enriched surface region of these seeds then undergoes spinodal decomposition, forming carbon-rich, α''-ordered clusters and a carbon-depleted disordered ferrite matrix, as outlined in Section 1.

To understand the evolving morphology of the carbon clusters, it is important to consider that the decomposition process does not initiate in a fixed, well-defined 3D bulk state. Instead, it occurs in the surface layer of the growing film, with film growth and microstructural evolution proceeding simultaneously. In this scenario, the first decomposing layer establishes concentration fluctuations that, with continued film growth, evolve into α''-ordered clusters. These clusters develop an out-of-plane plate-like morphology (Figure 6**c, f**) due to the layered growth of the film, as each new layer inherits the clustering pattern of the layer below. The ring-like arrangement of the clusters (Figure 6**d**) is governed by diffusion distances of carbon within the surface layer and may even result in nested rings. This mechanism is supported by the fact that carbon atoms diffuse fast enough in the surface layer to bridge the average cluster spacing of 8(2) nm before a new α-iron layer could grow, as outlined in Supplementary Note 3.

Parallels to cluster formation in tempered Fe-C martensite

The average cluster composition of 10–12 at.% C (cf. Figure 6**e**) closely matches the stoichiometry of α''-$Fe_{16}C_2$ clusters (~11 at.% C), which are observed across a range of differently annealed[4] Fe–C–X alloys (Table 2). These include systems as diverse as tempered martensitic [28] and bainitic [27] Fe–C–X alloys, aged martensitic Fe–Ni–C alloys [26], and even aged low-carbon ferritic steels [80]. These compositional parallels support our view that cluster formation during film deposition proceeds via the same spinodal decomposition mechanism that is well established for tempered martensites (see Section 1). Furthermore, our data reinforces the view—proposed by Morsdorf et al. [28]—that spinodal decomposition-driven carbon clustering is a ubiquitous phenomenon in Fe–C solid solutions. This interpretation is particularly compelling given that the mid-carbon films studied here are virtually free of substitutional alloying elements and contain carbon as the sole significant interstitial. Moreover, our findings show that this mechanism remains active even under high supersaturations of 8.0(3) at.% C.

4.1.3. Nanocarbide precipitation from carbon clusters

The observed nanofaceted regions with peak carbon concentrations of 27 to 31 at.% C (Figure 7) strongly suggest that some α'' clusters have already partially transformed into nanosized faceted carbides. This interpretation is based on three key arguments: (1) the observed concentrations fall within the nominal composition ranges of transitional ε-carbides ($Fe_{2\text{-}3}C$, 25–33.3 at.% C)[5] [82,83] and η-carbide (Fe_2C, 33.3 at.% C) [84]; (2) these carbides are known to form between 80 and 150 °C [24,25,85–88], consistent with our deposition temperatures (80–120 °C); and (3) carbon-rich clusters are widely accepted as precursors to carbide formation [19,28,63,89,90].

Our APT profiles suggest that the nanocarbides are plate-shaped with a thickness of ~0.6(2) nm and lateral extents of ~3 nm (twice the probing radius, see Figure 7). These dimensions closely match recent HR-STEM observations: Lu et al. [63] reported η-carbides with a thickness of 1.5(7) nm and nanofacet lengths of 3.1(4) nm, while Kawahara et al. [90] identified sub-2 nm ε-carbide structures embedded in α'' clusters. The nanoscale size of these embryonic carbides could also explain why they did not appear in our (S)TEM analysis, nor in XRD (cf. Supplementary **Figure SI 3**), as their volume fraction was likely too low for detection. While we cannot unambiguously determine the exact carbide type or structure from APT alone, the combination of composition, shape, and scale provides strong evidence that we are capturing the onset of carbide precipitation. These findings reinforce the prevailing view that carbon-rich clusters act as nucleation sites for transitional carbides in supersaturated Fe–C alloys.

4.1.4. Coupling of cluster formation and nanograin evolution

The striking match between the spacing of the carbon clusters (Figure 6) and the size of the columnar nanograins (Figure 2**b**) strongly suggests a coupling between cluster formation and nanograin evolution. We propose that this coupling occurs in two key ways.

First, the elevated carbon content in the α'' clusters can significantly lower the formation enthalpies of defects through the Gibbs adsorption effect [5,91]. At extreme supersaturation levels, these enthalpies may even become negative, creating conditions where the chemical driving force exerted by the solutes can overcompensate for the energy required to create a defect [5,92]. Under such conditions, the formation of highly decorated defects becomes energetically favorable, and the system spontaneously forms them — an effect recently termed chemically driven defect formation [92]. In our case, the carbon supersaturation within α'' clusters may trigger the spontaneous formation of low-angle grain boundaries, leading to the co-evolution of ferrite nanograins. One might envision the clusters as precursors, gradually accumulating carbon until chemically driven defect formation sets in — effectively imprinting the cluster distribution onto the emerging grain structure.

Second, the tetragonal distortion of the α'' clusters induces local strain at their coherent interfaces with the α-Fe matrix [90], which may further reduce the energetic cost of defect formation. Recent studies on ternary carbide formation in microalloyed steels—such as (Ti,Mo)C and (V,N)C—suggest that the development of defects like misfit dislocations and twin boundaries is a critical step in the transformation from coherent embryo clusters to semicoherent nanocarbides, accommodating the lattice mismatch at incoherent interfaces [93,94]. A similar mechanism may apply to the nanocarbides observed within the carbon clusters in our films, further illustrating the close interplay between nanoscale heterogeneities (e.g., clusters and nanoprecipitates) and structural defects.

Together, these two effects — chemical and mechanical — provide a compelling mechanism linking the evolution of nanograins to the carbon cluster architecture established during surface-layer spinodal decomposition.

4.2. Thermodynamics of Fe-C thin films

To explore the thermodynamic principles underlying film microstructures across different compositions, we propose free energy curves for disordered α-Fe, α''-ordered Fe, and amorphous Fe-C, based on the observed microstructures (Figure 9). The qualitative behavior of these curves is informed by Thermocalc simulations from Fillon et al. [41] for

[4] Differently annealed encompasses tempered, auto-tempered, and aged states. Tempering refers to deliberate short-term annealing of martensite, auto-tempering to cluster formation during cooling immediately after quenching (at still-elevated temperatures), and aging to long-term thermal exposure, often at lower temperatures.

[5] The exact composition of ε-carbide is still a matter of discussion, with proposed compositions ranging from Fe_2C to Fe_3C [81,82].

Table 2
Carbon cluster compositions in aged and tempered martensitic Fe-C-X alloys collected from literature.

Ref.	Material	M_S [°C]	C [at.%]	T [°C]	Time [h]	Cluster comp. [at.% C]
[26]	Fe–24Ni–1.85C	-50	1.85	RT	40 000	12(1)
[29]	Fe–1.83Mn–0.49Si– 0.19Cr–0.97C	407	0.97	RT	720 – 1440	> 10
[80]	Low C ferritic steel	-	0.21	50	240	10 – 12
[27]	Fe–1.32Mn–2.78Si–1.06Cr–0.09Ni–0.13 Mo–2.96C	200	2.96	auto-tempered		11.4(4)
[28]	Fe–2.52Mn–0.37Si–0.21Cr–1.04C	337	1.04	auto-tempered		11(3)

Compositions in at.% and Fe as balance; **RT**: room temperature; **M_S**: martensite start temperature

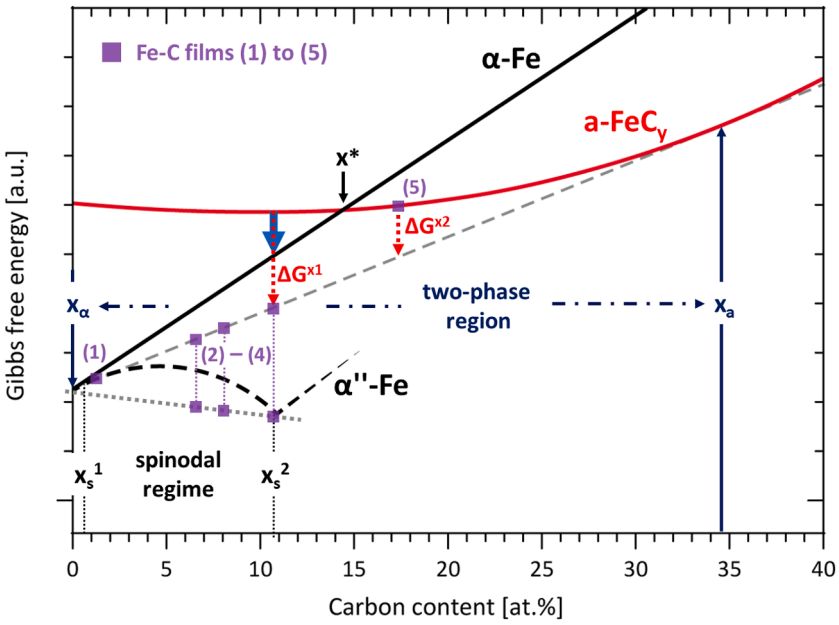

Figure 9. Proposed free energy curves for Fe-C at 100°C (deposition temperature) in the absence of carbides. The energy landscape is dominated by the two-phase region between ferrite (α-Fe, black curve) and amorphous Fe-C (a-FeC_y, red curve) and the miscibility gap (dashed black curve) between ferrite and carbon-ordered α''-$Fe_{16}C_2$. The positions of our films (1) to (5) relative to these equilibria are marked by light purple square symbols. For films (2) to (4), the upper symbols correspond to the bottom part of these films (amorphous interlayer and ferrite seeds), while the lower symbols correspond to their upper section (columnar ferrite and carbon clusters). Transformation paths from the amorphous phase to crystalline ferrite are indicated with arrows (blue: polymorphic transformation; red-dashed: nucleation involving chemical decomposition).

ferrite and amorphous Fe-C (red and black curves), and from Naraghi et al. [21] for α''-ordered Fe (black dashed curve). In the absence of carbide phases, the microstructural evolution of the Fe-C films is controlled by the two-phase region between amorphous Fe-C and crystalline ferrite (grey dashed common tangent) and by a miscibility gap formed between pure ferrite and α''-ordered Fe (grey dotted common tangent). We first examine these two regions separately (Sections 4.2.1 and 4.2.2), before discussing the transformation pathways that likely shaped the complex microstructure of the mid-carbon films (Section 4.2.3).

4.2.1. Two-phase region between α-Fe and amorphous FeC_y

The two-phase equilibrium between amorphous Fe-C and ferrite without carbide formation has been reported by several authors [41, 95–98] and is consistent with our observations of an amorphous interlayer with embedded ferrite seeds in the mid-carbon films (2) to (4). The exact values of the terminal solubilities x_α and x_a are not clear. In our case, we obtained a fully crystalline film with 1.32 at.% C (film 1) and a homogeneous amorphous film with 17.3 at.% C (film 5). By contrast, Fillon et al. [41] found solubility limits below 0.04 at.% C and above 24.7 at.% C in crystallization experiments. Of course, our samples may not have reached local equilibrium. For instance, as-deposited fully amorphous films with carbon concentrations between 13.6(1) at.% and 22 at.% C, began to precipitate ferrite when annealed at sufficiently high temperatures [41,97]. Moreover, crystalline films at the lower concentration end, such as film (1), may accommodate a fraction of carbon segregated at extended defects. This excess, which can be a few 0.1 at.% C [99,100], must be accounted for when evaluating the local equilibrium between ferrite and amorphous Fe-C.

Amorphously growing films within this two-phase region can lower their free energy by precipitating ferrite, while enriching the amorphous phase towards x_a (Figure 9, red dashed arrows). Up to x*, the cross-over of the a-FeC_y and α-Fe curve (the T_0 point), this may even proceed by forming ferrite without chemical partitioning (polymorphic transformation, blue solid arrow). However, the nucleation and growth of ferrite requires thermal activation. Since the driving force for ferrite formation decreases with increasing carbon content (see red arrows, ΔG^{x1} and ΔG^{x2}), the high carbon films, such as film (5), remain amorphous during low-temperature deposition and during storage at room temperature. In this sense, the mid-carbon films (2) to (4) can be seen as near-critical cases, where the chosen combination of carbon content (6.6 < x < 10.9 at.% C) and deposition temperature (80 to 120°C) was just sufficient to permit crystallization during deposition. The thickness of the retained amorphous interlayer in these films reflects the state that could be attained during deposition before the increase in carbon content of the amorphous phase caused the cessation of further ferrite growth into the interlayer (cf. Section 4.1.1). Consistent with this, we observed an increase in interlayer thickness with the overall carbon content of the mid carbon films (cf. Figure 2).

4.2.2. Miscibility gap between α-Fe and α''-$Fe_{16}C_2$

Carbon-enriched ferrite is predicted to lower its free energy by spinodal decomposition into carbon-rich bct α''-$Fe_{16}C_2$ clusters and a carbon-lean bcc matrix in the concentration range of 0.8 to about 11 at.% C [21]. The bounding compositions occur at the two inflections points of the α''-curve at x_s^1 at 0.8 at.% C and x_s^2 near 11 at.% C in Figure 9. Below 0.8 at.% C, the α-Fe and α''-Fe curves are identical and the equilibrium state is homogeneous. Our data supports the existence of a miscibility gap at free energies below that of the tie-line between the amorphous phase and ferrite (grey dashed line in Figure 9). This is based on two key observations: (1) once the primary ferrite seeds begin to develop carbon clusters, the surrounding amorphous Fe-C regions disappear entirely (Figure 2**e**), and (2) aside from the interlayer, no additional amorphous areas were observed (Figure 4).

4.2.3. Transformation path mid-carbon films

The fact that the amorphous phase is observed in the lower portions of the films and that the more stable spinodally decomposed microstructure is not reached indicates that polymorphic precipitation of ferrite is somehow suppressed, and the ferrite nuclei that form contain less than 0.8 at.% C. In this scenario, cluster formation would not take place, as the nuclei would fall outside the spinodal decomposition range, leading to a phase balance between amorphous Fe-C and nearly pure ferrite. This scenario is consistent with the crystallization experiments by Fillon et al. [41], where the ferrite seeds that formed within the amorphous film contained almost no carbon (0.04 at.% C) and showed no evidence of cluster formation in APT.

Cluster formation begins only after the primary ferrite seeds at the film surface have grown sufficiently large, as described in Section 4.1.2. At this stage, the amorphous phase is no longer fully accessible to incoming carbon atoms, causing some to become trapped within the growing seeds. This forced intake quickly enriches the seeds beyond 0.8 at.% C, triggering spinodal cluster formation, which ultimately leads to the fully ferritic microstructure in the upper part of the mid-carbon films.

4.3. Texture evolution of mid-carbon Fe-C films

Our 4D-STEM and X-ray texture analysis reveal that the mid-carbon films undergo a texture change from an initially thin layer of {110} out-of-plane (oop) ordered crystallites into a combination of {111} and {031} oop ordered crystallites as growth proceeds. The initial {110} oop texture can be attributed to the fraction of α-Fe seeds that nucleate at the film's surface. These seeds preferentially form with {110} planes aligned oop, as {110} planes in bcc iron have the lowest surface energy [101,102]. Consistent with this, pure iron films have been found to form slightly {110} oop textured films on amorphous substrates [103]. However, to our knowledge, neither the transition to nor the emergence of a mixed {111} and {031} oop fiber texture in Fe-C films has been reported previously.

The 4D-STEM data (Figure 5) suggests that the {110} grains are occluded by adjacent grains, which likely experienced faster growth. This phenomenon is well-documented in low-temperature deposited fcc films [104], where anisotropies in growth velocities arise because the thermodynamic driving force varies with the specific grain orientation through surface/interface energies and strain energies. The competition of these two energies largely determines the final film texture. In our case, variations in strain energy contributions are expected, as the Young's modulus of bcc iron is anisotropic [105][6]. Thus, while the initial {110} oop texture minimizes surface energy, the mixed {111} and {031} oop fiber texture likely develops to reduce strain when the growing grains meet. A potential source of this strain could be the α'' clusters, where carbon ordering induces local tetragonal lattice distortions [90,106,107].

4.4. Hardness of the nanostructured mid-carbon films

We found that the nanostructured mid-carbon films exhibit a nanoindentation hardness of 21(2) GPa or higher (Figure 8). This is significantly harder than bulk martensite with a comparable carbon content (Figure 10**a**) and consistent with the findings of Dahlgren et al. [33], who observed in macroscopic hardness testing that sputtered Fe-C films generally achieve higher Vickers hardness than martensite quenched from the same targets (Figure 10**b**). The mid-carbon films almost outperform advanced nanostructured steels produced by severe plastic deformation (SPD). For instance, cold-drawn pearlite wires with a near-theoretical tensile strength σ of 7 GPa [6] reach a hardness H of ~21 GPa, based on the well-established relation $H \approx 3\sigma$ [108] (Figure 10**a,** red dot).

The remarkable hardness of the mid-carbon films — and its close match to that of cold-drawn pearlite — can be rationalized by revisiting the underlying strengthening mechanisms. In cold-drawn pearlite, the near-theoretical strength arises from a carbon-decorated columnar nanograin structure [6,110]: ultrafine grains (<10 nm) impede dislocation motion via Hall–Petch strengthening, while the columnar grain morphology restricts grain boundary sliding. The mid-carbon films exhibit comparable features — columnar ferrite nanograins decorated with carbon clusters — offering similar resistance to plastic deformation. Additional contributions likely stem from (1) high interstitial carbon concentrations within the ferrite grains (~5.1 at.% C, see Figure 6**e**), which impedes dislocation motion via solute drag [111,112], and (2) carbon clusters and nanocarbides at grain boundaries, which serve as strong obstacles to dislocation propagation. Notably, cluster strengthening has recently emerged as a promising strategy in steel design, though the dominant mechanism remains under debate [113,114].

Thin films differ from bulk materials in several respects, complicating the direct comparability and applicability of results. For example, substrate effects can compromise hardness measurements if indentation depths exceed 10% of the film thickness [68,69], which we avoided in this study (cf. Section 3.4). Moreover, thin film properties are often governed by surface and interface effects, which play a less dominant role in bulk materials. However, many advanced steels derive their exceptional properties from nanoscale features and interface-controlled mechanisms [115,116], making them structurally and functionally similar to thin films in this regard. Therefore, thin films serve as valuable model systems for nanostructured Fe-C alloys, and the insights gained in this study are relevant to bulk materials produced under extreme processing conditions such as SPD or rapid solidification. Beyond their role as model systems, the Fe-C films studied here also show promise as functional hard coatings: their nanostructure forms in situ during deposition, eliminating the need for additional processing steps and offering a straightforward, energy-efficient alternative to conventional bulk nanostructuring techniques.

5. Conclusions

This study reveals how carbon critically controls the microstructural evolution of Fe-C thin films synthesized by sputter deposition. By tuning the carbon content, we demonstrate precise control over the resulting film microstructure — from fully crystalline to fully amorphous films. At intermediate carbon levels, a two-step growth process emerges, leading to complex nanostructures with remarkable mechanical properties.

Key findings:

- A concentration-dependent nucleation barrier determines whether the films crystallize during growth or remain amorphous.

[6] The <111> directions in bcc α-Fe are the stiffest, with a Young's modulus of 293 GPa and the <100> directions are the softest with 141 GPa.

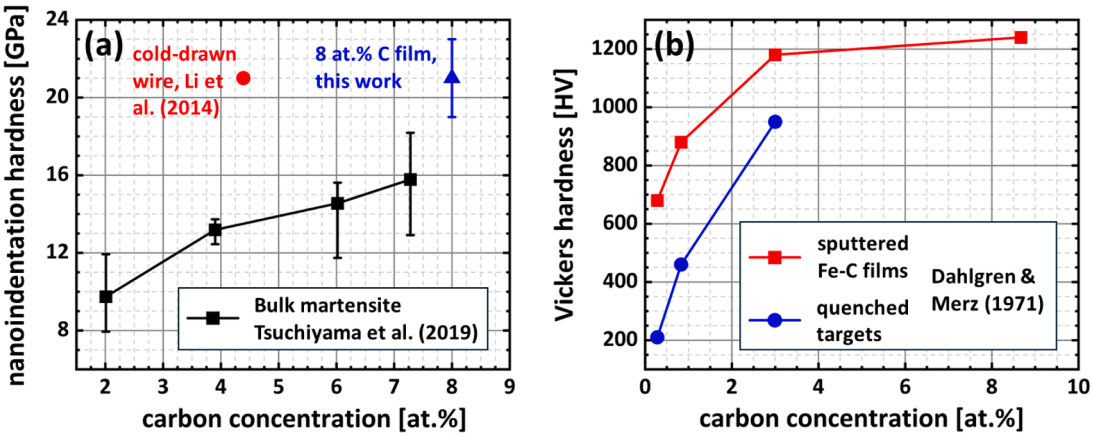

Figure 10. Nanoindentation (a) and Vickers hardness (b) of various high-carbon Fe-C materials. (**a**) Nanoindentation hardness of the examined 8 at.% C film (blue triangle), bulk martensite with similar carbon content (black squares, data from [109]), and a theoretical estimate using $H \approx 3\sigma$ for cold-drawn pearlite (red dot, data from [6]). **(b)** Vickers hardness of thick crystalline Fe–C films (127–686 μm) produced by sputter deposition, compared to martensite obtained from the corresponding sputter targets by quenching (data from [33]).

- At intermediate carbon contents (6.6 to 10.9 at.% C), a two-step growth process occurs:

  Stage I: formation of an amorphous Fe-C interlayer, followed by nucleation and growth of columnar α-Fe grains.

  Stage II: once the ferrite grains exceed a critical size, carbon becomes trapped and locally supersaturated, triggering spinodal decomposition near the advancing film surface.
  - This leads to the formation of nanoscale, plate-like carbon-rich clusters (~α''-$Fe_{16}C_2$), arranged in in-plane rings and spaced 5–10 nm apart.
  - These carbon clusters co-evolve with columnar ferrite nanograins and ultimately appear aligned along their boundaries. We propose that carbon aggregation in clusters chemically drives nanograin formation via the Gibbs adsorption effect, while the resulting defects may also help relax elastic strain.
- A texture change accompanies the transition between growth stages — from {110} oop at the bottom (driven by surface energy minimization) to a mixed {111} and {031} oop fiber texture that dominates most of the crystalline film (attributed to strain energy minimization).
- The carbon clusters exhibit nanoscale concentration modulations reaching 27–31 at.% C, indicating the onset of transitional carbide formation (η or ε) and reinforcing their role as carbide precursors.
- The mid-carbon films achieve a nanostructure and mechanical performance comparable to advanced bulk Fe-C materials — without the need for post-processing.

These findings deepen our understanding of non-equilibrium microstructure formation in carbon-supersaturated Fe-C systems and demonstrate that sputter deposition offers a direct, energy-efficient route to nanostructured materials. As such, these thin films not only serve as model systems for bulk alloys formed under extreme processing conditions, but also show promise as high-hardness coatings.

Declaration of Generative AI and AI-assisted technologies in the writing process

During the preparation of this work the authors used ChatGPT, a language model developed by OpenAI, in order to enhance readability and language. After using this tool, the authors reviewed and edited the content as needed and take full responsibility for the content of the publication.

CRediT authorship contribution statement

J. Arlt: Writing – review & editing, Writing – original draft, Visualization, Project administration, Methodology, Investigation, Formal analysis. **T. Meyer:** Writing – review & editing, Visualization, Methodology, Investigation, Formal analysis. **M. Roscher:** Visualization, Resources, Investigation. **T. Brede:** Validation, Resources, Data curation. **C. Borchers:** Validation, Resources, Data curation. **T.M. Schwarz:** Writing – review & editing, Methodology, Formal analysis. **P. Stender:** Supervision, Methodology, Formal analysis. **A. Pundt:** Writing – review & editing, Supervision, Conceptualization. **C.A. Volkert:** Writing – review & editing, Project administration, Funding acquisition, Conceptualization.

Declaration of competing interest

The authors declare that they have no known competing financial interests or personal relationships that could have appeared to influence the work reported in this paper.

Acknowledgements

We thank Dr. Andreas Kronz at the Geowissenschaftliches Zentrum, Göttingen University, for conducting and discussing the electron probe micro analysis measurements. We are grateful to Prof. Guido Schmitz for allowing us to use the atom probe and other laboratory equipment at the Institute for Materials Science in Stuttgart. We also thank Dr. Helmut Klein for helping to analyze and discuss the pole figure measurements, with Natalie Oettinger assisting the process, and My Nguyen for conducting the nanoindentation measurements. Additionally, we appreciate Prof. Isabella Gallino for the fruitful discussions regarding the amorphous Fe-C layer.

The use of equipment in the Göttingen Laboratory for Correlative Light and Electron Microscopy (GoeLEM – www.mineralogie.uni-goettingen.de) and the "Collaborative Laboratory and User Facility for Electron Microscopy" (CLUE – www.clue.physik.uni-goettingen.de) are gratefully acknowledged.

Funding from the Deutsche Forschungsgemeinschaft (DFG) within the Research Group „Energy Landscapes and Structure in Ion Conducting Solids" under Project Number 428906592 is gratefully acknowledged.

Supplementary materials

Supplementary material associated with this article can be found, in the online version, at doi:10.1016/j.actamat.2025.121124.

References

[1] D. Raabe, Z. Li, D. Ponge, Metastability alloy design, MRS Bull 44 (2019) 266–272, https://doi.org/10.1557/mrs.2019.72.

[2] Y. Chen, Z. Lai, X. Zhang, Z. Fan, Q. He, C. Tan, H. Zhang, Phase engineering of nanomaterials, Nat Rev Chem 4 (2020) 243–256, https://doi.org/10.1038/s41570-020-0173-4.

[3] R. Ding, Y. Yao, B. Sun, G. Liu, J. He, T. Li, X. Wan, Z. Dai, D. Ponge, D. Raabe, C. Zhang, A. Godfrey, G. Miyamoto, T. Furuhara, Z. Yang, S. van der Zwaag, H. Chen, Chemical boundary engineering: A new route toward lean, ultrastrong yet ductile steels, Science Advances 6 (2020) eaay1430, https://doi.org/10.1126/sciadv.aay1430.

[4] R.Z. Valiev, B. Straumal, T.G. Langdon, Using Severe Plastic Deformation to Produce Nanostructured Materials with Superior Properties, Annu. Rev. Mater. Res. 52 (2022) 357–382, https://doi.org/10.1146/annurev-matsci-081720-123248.

[5] R. Kirchheim, Reducing grain boundary, dislocation line and vacancy formation energies by solute segregation. I. Theoretical background, Acta Materialia 55 (2007) 5129–5138, https://doi.org/10.1016/j.actamat.2007.05.047.

[6] Y. Li, D. Raabe, M. Herbig, P.-P. Choi, S. Goto, A. Kostka, H. Yarita, C. Borchers, R. Kirchheim, Segregation Stabilizes Nanocrystalline Bulk Steel with Near Theoretical Strength, Phys. Rev. Lett. 113 (2014) 106104, https://doi.org/10.1103/PhysRevLett.113.106104.

[7] Y.Z. Chen, A. Herz, Y.J. Li, C. Borchers, P. Choi, D. Raabe, R. Kirchheim, Nanocrystalline Fe–C alloys produced by ball milling of iron and graphite, Acta Materialia 61 (2013) 3172–3185, https://doi.org/10.1016/j.actamat.2013.02.006.

[8] H. Hidaka, K. Kawasaki, T. Tsuchiyama, S. Takaki, Effect of Carbon on Nano-Crystallization in Steel during Mechanical Milling Treatment, Materials Transactions 44 (2003) 1912–1918, https://doi.org/10.2320/matertrans.44.1912.

[9] J. Speer, D.K. Matlock, B.C. De Cooman, J.G. Schroth, Carbon partitioning into austenite after martensite transformation, Acta Materialia 51 (2003) 2611–2622, https://doi.org/10.1016/S1359-6454(03)00059-4.

[10] J.G. Speer, F.C.R. Assunção, D.K. Matlock, D.V. Edmonds, The "quenching and partitioning" process: background and recent progress, Mat. Res. 8 (2005) 417–423, https://doi.org/10.1590/S1516-14392005000400010.

[11] F. Hu, K.M. Wu, Nanostructured high-carbon dual-phase steels, Scripta Materialia 65 (2011) 351–354, https://doi.org/10.1016/j.scriptamat.2011.05.004.

[12] T.Y.H. X.D. Wang, N. Zhong, Y.H. Rong, Z.Y. Xu, L. Wang, Novel ultrahigh-strength nanolath martensitic steel by quenching–partitioning–tempering process Journal of Materials Research 24 (2009) 260–267, https://doi.org/10.1557/JMR.2009.0029.

[13] D. Raabe, D. Ponge, O. Dmitrieva, B. Sander, Nanoprecipitate-hardened 1.5 GPa steels with unexpected high ductility, Scripta Materialia 60 (2009) 1141–1144, https://doi.org/10.1016/j.scriptamat.2009.02.062.

[14] S. Jiang, H. Wang, Y. Wu, X. Liu, H. Chen, M. Yao, B. Gault, D. Ponge, D. Raabe, A. Hirata, M. Chen, Y. Wang, Z. Lu, Ultrastrong steel via minimal lattice misfit and high-density nanoprecipitation, Nature 544 (2017) 460–464, https://doi.org/10.1038/nature22032.

[15] A. Udyansky, J. Von Pezold, V.N. Bugaev, M. Friák, J. Neugebauer, Interplay between long-range elastic and short-range chemical interactions in Fe-C martensite formation, Phys. Rev. B 79 (2009) 224112, https://doi.org/10.1103/PhysRevB.79.224112.

[16] X. Zhang, H. Wang, T. Hickel, J. Rogal, Y. Li, J. Neugebauer, Mechanism of collective interstitial ordering in Fe–C alloys, Nat. Mater. 19 (2020) 849–854, https://doi.org/10.1038/s41563-020-0677-9.

[17] C. Zener, Theory of Strain Interaction of Solute Atoms, Phys. Rev. 74 (1948) 639–647, https://doi.org/10.1103/PhysRev.74.639.

[18] L. Cheng, A. Böttger, Th.H. de Keijser, E.J. Mittemeijer, Lattice parameters of iron-carbon and iron-nitrogen martensites and austenites, Scripta Metallurgica et Materialia 24 (1990) 509–514, https://doi.org/10.1016/0956-716X(90)90192-J.

[19] K.A. Taylor, L. Chang, G.B. Olson, G.D.W. Smith, M. Cohen, J.B.V. Sande, Spinodal decomposition during aging of Fe-Ni-C martensites, Metall Trans A 20 (1989) 2717–2737, https://doi.org/10.1007/BF02670166.

[20] C.W. Sinclair, M. Perez, R.G.A. Veiga, A. Weck, Molecular dynamics study of the ordering of carbon in highly supersaturated α -Fe, Phys. Rev. B 81 (2010) 224204, https://doi.org/10.1103/PhysRevB.81.224204.

[21] R. Naraghi, M. Selleby, J. Ågren, Thermodynamics of stable and metastable structures in Fe–C system, Calphad 46 (2014) 148–158, https://doi.org/10.1016/j.calphad.2014.03.004.

[22] J. Merlin, P. Merle, S. Garnier, M. Bouzekri, M. Soler, Experimental determination of the carbon solubility limit in ferritic steels, Metall Mater Trans A 35 (2004) 1655–1661, https://doi.org/10.1007/s11661-004-0074-z.

[23] M. Kusunoki, S. Nagakura, Modulated structure of iron–carbon martensite studied by electron microscopy and diffraction, J Appl Cryst 14 (1981) 329–336, https://doi.org/10.1107/S0021889881009485.

[24] S. Nagakura, Y. Hirotsu, M. Kusunoki, T. Suzuki, Y. Nakamura, Crystallographic study of the tempering of martensitic carbon steel by electron microscopy and diffraction, Metall Trans A 14 (1983) 1025–1031, https://doi.org/10.1007/BF02670441.

[25] K. Han, M.J. van Genderen, A. Böttger, H.W. Zandbergen, E.J. Mittemeijer, Initial stages of Fe-C martensite decomposition, Philosophical Magazine A 81 (2001) 741–757, https://doi.org/10.1080/01418610108212169.

[26] P. Maugis, F. Danoix, M. Dumont, S. Curelea, S. Cazottes, H. Zapolsky, M. Gouné, Carbon diffusivity and kinetics of spinodal decomposition of martensite in a model Fe-Ni-C alloy, Materials Letters 214 (2018) 213–216, https://doi.org/10.1016/j.matlet.2017.12.007.

[27] R. Rementeria, C. Capdevila, R. Domínguez-Reyes, J.D. Poplawsky, W. Guo, E. Urones-Garrote, C. Garcia-Mateo, F.G. Caballero, Carbon Clustering in Low-Temperature Bainite, Metall Mater Trans A 49 (2018) 5277–5287, https://doi.org/10.1007/s11661-018-4899-2.

[28] L. Morsdorf, E. Emelina, B. Gault, M. Herbig, C.C. Tasan, Carbon redistribution in quenched and tempered lath martensite, Acta Materialia 205 (2021) 116521, https://doi.org/10.1016/j.actamat.2020.116521.

[29] J. Macchi, J. Teixeira, F. Danoix, G. Geandier, S. Denis, F. Bonnet, S.Y.P. Allain, Impact of carbon segregation on transition carbides and cementite precipitation during tempering of low carbon steels: Experiments and modeling, Acta Materialia 272 (2024) 119919, https://doi.org/10.1016/j.actamat.2024.119919.

[30] L. Morsdorf, C.C. Tasan, D. Ponge, D. Raabe, 3D structural and atomic-scale analysis of lath martensite: Effect of the transformation sequence, Acta Materialia 95 (2015) 366–377, https://doi.org/10.1016/j.actamat.2015.05.023.

[31] B. Hutchinson, J. Hagström, O. Karlsson, D. Lindell, M. Tornberg, F. Lindberg, M. Thuvander, Microstructures and hardness of as-quenched martensites (0.1–0.5%C), Acta Materialia 59 (2011) 5845–5858, https://doi.org/10.1016/j.actamat.2011.05.061.

[32] F. Niessen, D. Apel, F. Danoix, J. Hald, M.A.J. Somers, Evolution of substructure in low-interstitial martensitic stainless steel during tempering, Materials Characterization 167 (2020) 110494, https://doi.org/10.1016/j.matchar.2020.110494.

[33] S.D. Dahlgren, M.D. Merz, Solid solutions in sputter-deposits of iron with 0 to 5 Wt Pct C, Metall Mater Trans B 2 (1971) 1753–1760, https://doi.org/10.1007/BF02913402.

[34] E. Bauer-Grosse, G.L. Caër, Structural evolution of sputtered amorphous $Fe_{1-x}C_x$ films for $0.19 \leq x \leq 0.49$, Philosophical Magazine B 56 (1987) 485–500, https://doi.org/10.1080/13642818708221334.

[35] E. Bauer-Grosse, A. Aouni, Glass-forming range and glass thermal stability in binary 3d TM–C systems, Journal of Non-Crystalline Solids 353 (2007) 3644–3649, https://doi.org/10.1016/j.jnoncrysol.2007.05.127.

[36] A. Weck, C.W. Sinclair, C.P. Scott, C. Maunder, Supersaturated α-iron in vapour-deposited Fe–C thin films, J Mater Sci 47 (2012) 6939–6947, https://doi.org/10.1007/s10853-012-6641-6.

[37] A. Furlan, U. Jansson, J. Lu, L. Hultman, M. Magnuson, Structure and bonding in amorphous iron carbide thin films, J. Phys.: Condens. Matter 27 (2015) 045002, https://doi.org/10.1088/0953-8984/27/4/045002.

[38] I. Jouanny, V. Demange, J. Ghanbaja, E. Bauer-Grosse, Structural characterization of Fe–C coatings prepared by reactive triode-magnetron sputtering, Journal of Materials Research 25 (2010) 1859–1869, https://doi.org/10.1557/JMR.2010.0241.

[39] D. Babonneau, J. Briatico, F. Petroff, T. Cabioc'h, A. Naudon, Structural and magnetic properties of Fe_x–C_{1-x} nanocomposite thin films, Journal of Applied Physics 87 (2000) 3432–3443, https://doi.org/10.1063/1.372363.

[40] D. Babonneau, T. Cabioc'h, M.-F. Denanot, A. Naudon, Microstructural study of a C–Fe alloy synthesized by ion-beam sputtering co-deposition, Appl. Phys. Lett. 74 (1999) 800–802, https://doi.org/10.1063/1.123372.

[41] A. Fillon, X. Sauvage, B. Lawrence, C. Sinclair, M. Perez, A. Weck, E. Cantergiani, T. Epicier, C.P. Scott, On the direct nucleation and growth of ferrite and cementite without austenite, Scripta Materialia 95 (2015) 35–38, https://doi.org/10.1016/j.scriptamat.2014.09.025.

[42] M.C. Tiegel, M.L. Martin, A.K. Lehmberg, M. Deutges, C. Borchers, R. Kirchheim, Crack and blister initiation and growth in purified iron due to hydrogen loading, Acta Materialia 115 (2016) 24–34, https://doi.org/10.1016/j.actamat.2016.05.034.

[43] J.S. Duerr, R.E. Ogilvie, Electron probe microdetermination of carbon in ferrous alloys, Anal. Chem. 44 (1972) 2361–2367, https://doi.org/10.1021/ac60322a012.

[44] Z.-Q. Liu, G. Miyamoto, Z.-G. Yang, T. Furuhara, Direct measurement of carbon enrichment during austenite to ferrite transformation in hypoeutectoid Fe–2Mn–C alloys, Acta Materialia 61 (2013) 3120–3129, https://doi.org/10.1016/j.actamat.2013.02.003.

[45] P.T. Pinard, A. Schwedt, A. Ramazani, U. Prahl, S. Richter, Characterization of Dual-Phase Steel Microstructure by Combined Submicrometer EBSD and EPMA Carbon Measurements, Microscopy and Microanalysis 19 (2013) 996–1006, https://doi.org/10.1017/S1431927613001554.

[46] Y. Xia, G. Miyamoto, Z.G. Yang, C. Zhang, T. Furuhara, Direct measurement of carbon enrichment in the incomplete bainite transformation in Mo added low carbon steels, Acta Materialia 91 (2015) 10–18, https://doi.org/10.1016/j.actamat.2015.03.021.

[47] C.A. Goodrich, J.M. Bird, Formation of Iron-Carbon Alloys in Basaltic Magma at Uivfaq, Disko Island: The Role of Carbon in Mafic Magmas, The Journal of Geology 93 (1985) 475–492, https://doi.org/10.1086/628967.

[48] W.C. Oliver, G.M. Pharr, Measurement of hardness and elastic modulus by instrumented indentation: Advances in understanding and refinements to methodology, Journal of Materials Research 19 (2004) 3–20, https://doi.org/10.1557/jmr.2004.19.1.3.

[49] W.C. Oliver, G.M. Pharr, An improved technique for determining hardness and elastic modulus using load and displacement sensing indentation experiments, Journal of Materials Research 7 (1992) 1564–1583, https://doi.org/10.1557/JMR.1992.1564.

[50] M.K. Miller, K.F. Russell, K. Thompson, R. Alvis, D.J. Larson, Review of Atom Probe FIB-Based Specimen Preparation Methods, Microsc Microanal 13 (2007) 428–436.

[51] K. Iakoubovskii, K. Mitsuishi, Y. Nakayama, K. Furuya, Thickness measurements with electron energy loss spectroscopy, Microscopy Research and Technique 71 (2008) 626–631, https://doi.org/10.1002/jemt.20597.

[52] T. Meyer, Dissertation, Georg-August Universität, Göttingen, 2020, p. 2021.

[53] R. Schlesiger, C. Oberdorfer, R. Würz, G. Greiwe, P. Stender, M. Artmeier, P. Pelka, F. Spaleck, G. Schmitz, Design of a laser-assisted tomographic atom probe at Münster University, Review of Scientific Instruments 81 (2010) 043703, https://doi.org/10.1063/1.3378674.

[54] P. Stender, I. Balla, Scito - APT Reconstruction Software, www.Inspico.eu.

[55] D.R. Kingham, The post-ionization of field evaporated ions: A theoretical explanation of multiple charge states, Surface Science 116 (1982) 273–301, https://doi.org/10.1016/0039-6028(82)90434-4.

[56] J.J. Hren, Specimen contamination in analytical electron microscopy: sources and solutions, Ultramicroscopy 3 (1978) 375–380.

[57] M. Thuvander, J. Weidow, J. Angseryd, L.K.L. Falk, F. Liu, M. Sonestedt, K. Stiller, H.-O. Andrén, Quantitative atom probe analysis of carbides, Ultramicroscopy 111 (2011) 604–608, https://doi.org/10.1016/j.ultramic.2010.12.024.

[58] F. Meisenkothen, E.B. Steel, T.J. Prosa, K.T. Henry, R.Prakash Kolli, Effects of detector dead-time on quantitative analyses involving boron and multi-hit detection events in atom probe tomography, Ultramicroscopy 159 (2015) 101–111, https://doi.org/10.1016/j.ultramic.2015.07.009.

[59] Z. Peng, F. Vurpillot, P.-P. Choi, Y. Li, D. Raabe, B. Gault, On the detection of multiple events in atom probe tomography, Ultramicroscopy 189 (2018) 54–60, https://doi.org/10.1016/j.ultramic.2018.03.018.

[60] Z. Peng, D. Zanuttini, B. Gervais, E. Jacquet, I. Blum, P.-P. Choi, D. Raabe, F. Vurpillot, B. Gault, Unraveling the Metastability of C_n^{2+} (n = 2–4) Clusters, J. Phys. Chem. Lett. 10 (2019) 581–588, https://doi.org/10.1021/acs.jpclett.8b03449.

[61] W. Sha, L. Chang, G.D.W. Smith, Liu Cheng, E.J. Mittemeijer, Some aspects of atom-probe analysis of Fe-C and Fe-N systems, Surface Science 266 (1992) 416–423, https://doi.org/10.1016/0039-6028(92)91055-G.

[62] Y.J. Li, P. Choi, C. Borchers, S. Westerkamp, S. Goto, D. Raabe, R. Kirchheim, Atomic-scale mechanisms of deformation-induced cementite decomposition in pearlite, Acta Materialia 59 (2011) 3965–3977, https://doi.org/10.1016/j.actamat.2011.03.022.

[63] W. Lu, M. Herbig, C.H. Liebscher, L. Morsdorf, R.K.W. Marceau, G. Dehm, D. Raabe, Formation of eta carbide in ferrous martensite by room temperature aging, Acta Materialia 158 (2018) 297–312, https://doi.org/10.1016/j.actamat.2018.07.071.

[64] M. Martyniuk, J. Antoszewski, B.A. Walmsley, C.A. Musca, J.M. Dell, Y.-G. Jung, B.R. Lawn, H. Huang, L. Faraone, Determination of mechanical properties of silicon nitride thin films using nanoindentation. Spaceborne Sensors II, SPIE, 2005, pp. 216–225, https://doi.org/10.1117/12.604245.

[65] D. Beegan, S. Chowdhury, M.T. Laugier, The nanoindentation behaviour of hard and soft films on silicon substrates, Thin Solid Films 466 (2004) 167–174, https://doi.org/10.1016/j.tsf.2004.03.006.

[66] J. Yan, H. Takahashi, J. Tamaki, X. Gai, H. Harada, J. Patten, Nanoindentation tests on diamond-machined silicon wafers, Applied Physics Letters 86 (2005) 181913, https://doi.org/10.1063/1.1924895.

[67] W. Zhang, J. Li, Y. Xing, X. Nie, F. Lang, S. Yang, X. Hou, C. Zhao, Experimental Study on the Thickness-Dependent Hardness of SiO_2 Thin Films Using Nanoindentation, Coatings 11 (2021) 23, https://doi.org/10.3390/coatings11010023.

[68] H. Bückle, Progress in Micro-Indentation Hardness Testing, Metallurgical Reviews 4 (1959) 49–100, https://doi.org/10.1179/095066059790421746.

[69] E. Broitman, Indentation Hardness Measurements at Macro-, Micro-, and Nanoscale: A Critical Overview, Tribol Lett 65 (2017) 23, https://doi.org/10.1007/s11249-016-0805-5.

[70] I. Gallino, R. Busch, Brief History of Metallic Glasses, in: I. Gallino, R. Busch (Eds.), Physical Metallurgy of Bulk Metallic Glass-Forming Liquids: Thermodynamic and Kinetic Concepts in Glass Formation, Springer Nature Switzerland, Cham, 2024, pp. 5–21, https://doi.org/10.1007/978-3-031-71536-5_2.

[71] M.D. Ediger, Perspective: Highly stable vapor-deposited glasses, The Journal of Chemical Physics 147 (2017) 210901, https://doi.org/10.1063/1.5006265.

[72] C. Rodriguez-Tinoco, M. Gonzalez-Silveira, M.A. Ramos, J. Rodriguez-Viejo, Ultrastable glasses: new perspectives for an old problem, Riv. Nuovo Cim. 45 (2022) 325–406, https://doi.org/10.1007/s40766-022-00029-y.

[73] C.R. Cao, Y.M. Lu, H.Y. Bai, W.H. Wang, High surface mobility and fast surface enhanced crystallization of metallic glass, Applied Physics Letters 107 (2015) 141606, https://doi.org/10.1063/1.4933036.

[74] X. Cao, H. Zhang, Y. Han, Release of free-volume bubbles by cooperative-rearrangement regions during the deposition growth of a colloidal glass, Nat Commun 8 (2017) 362, https://doi.org/10.1038/s41467-017-00428-4.

[75] G. Greczynski, L. Hultman, Impact of sample storage type on adventitious carbon and native oxide growth: X-ray photoelectron spectroscopy study, Vacuum 205 (2022) 111463, https://doi.org/10.1016/j.vacuum.2022.111463.

[76] L.H. Grey, H.-Y. Nie, M.C. Biesinger, Defining the nature of adventitious carbon and improving its merit as a charge correction reference for XPS, Applied Surface Science 653 (2024) 159319, https://doi.org/10.1016/j.apsusc.2024.159319.

[77] W. Chambron, F. Lancon, A. Chamberod, Carbon migration in the amorphous alloy Fe81B13.5Si3.5C2 as studied by magnetic anisotropy measurements, Journal of Non-Crystalline Solids 61–62 (1984) 895–900, https://doi.org/10.1016/0022-3093(84)90656-2.

[78] S. Soltani, J. Rottler, C.W. Sinclair, Carbon diffusion in concentrated Fe–C glasses, Modelling Simul. Mater. Sci. Eng. 29 (2021) 035003, https://doi.org/10.1088/1361-651X/abdc68.

[79] R.W.K. Honeycombe, H.K.D.H. Bhadeshia, Steels - Microstructure and Properties, 2nd ed., London, 1995.

[80] K. Ushioda, K. Takata, J. Takahashi, K. Kinoshita, H. Sawada, Changes in States of Carbon and Mechanical Properties with Aging at 50°C after Quenching in Low Carbon Steel, Mater. Trans. 61 (2020) 668–677, https://doi.org/10.2320/matertrans.MT-M2019351.

[81] W. Song, J. Von Appen, P. Choi, R. Dronskowski, D. Raabe, W. Bleck, Atomic-scale investigation of ε and θ precipitates in bainite in 100Cr6 bearing steel by atom probe tomography and ab initio calculations, Acta Materialia 61 (2013) 7582–7590, https://doi.org/10.1016/j.actamat.2013.08.051.

[82] S.A.J. Forsik, P.E.J. Rivera-Diaz-del-Castillo, Martensitic Steels: Epsilon Carbides in Tempered. Encyclopedia of Iron, Steel, and Their Alloys, Taylor and Francis, New York, 2016. http://www.crcnetbase.com/doi/book/10.1081/E-EISA. accessed July 25, 2024.

[83] K.H. Jack, Results of further X-ray structural investigations of the iron–carbon and iron–nitrogen systems and of related interstitial alloys, Acta Cryst 3 (1950) 392–394, https://doi.org/10.1107/S0365110X50001075.

[84] Y. Hirotsu, S. Nagakura, Crystal structure and morphology of the carbide precipitated from martensitic high carbon steel during the first stage of tempering, Acta Metallurgica 20 (1972) 645–655, https://doi.org/10.1016/0001-6160(72)90020-X.

[85] Y. Ohmori, I. Tamura, Epsilon carbide precipitation during tempering of plain carbon martensite, Metall Trans A 23 (1992) 2737–2751, https://doi.org/10.1007/BF02651753.

[86] M.J. Van Genderen, M. Isac, A. Böttger, E.J. Mittemeijer, Aging and tempering behavior of iron-nickel-carbon and iron-carbon martensite, Metall Mater Trans A 28 (1997) 545–561, https://doi.org/10.1007/s11661-997-0042-5.

[87] P.V. Morra, A.J. Böttger, E.J. Mittemeijer, Decomposition of Iron-based Martensite. A kinetic analysis by means of differential scanning calorimetry and dilatometry, Journal of Thermal Analysis and Calorimetry 64 (2001) 905–914, https://doi.org/10.1023/A:1011514727891.

[88] I. Tkalcec, C. Azcoitia, S. Crevoiserat, D. Mari, Tempering effects on a martensitic high carbon steel, Materials Science and Engineering: A 387–389 (2004) 352–356, https://doi.org/10.1016/j.msea.2004.02.072.

[89] S. Thompson, Further Observations of Linear Arrays of Transition-Iron-Carbide Precipitates in Tempered 4340 Steel, Metallogr. Microstruct. Anal. 7 (2018) 680–691, https://doi.org/10.1007/s13632-018-0492-8.

[90] Y. Kawahara, K. Kaneko, H. Sawada, J. Takahashi, Transition from carbon clusters to ε, θ-carbides in a quenched and aged low-carbon ferritic steel, Acta Materialia 252 (2023) 118919, https://doi.org/10.1016/j.actamat.2023.118919.

[91] J.W. Gibbs, The Collected Works of J. W. Gibbs, Longmans, Green and Company, New York, 1928.

[92] A. Tehranchi, S. Zhang, A. Zendegani, C. Scheu, T. Hickel, J. Neugebauer, Metastable defect phase diagrams as roadmap to tailor chemically driven defect formation, Acta Materialia 277 (2024) 120145, https://doi.org/10.1016/j.actamat.2024.120145.

[93] J. Wang, M. Weyland, I. Bikmukhametov, M.K. Miller, P.D. Hodgson, I. Timokhina, Transformation from cluster to nano-precipitate in microalloyed ferritic steel, Scripta Materialia 160 (2019) 53–57, https://doi.org/10.1016/j.scriptamat.2018.09.039.

[94] H. Wang, Y. Li, E. Detemple, G. Eggeler, Revealing the two-step nucleation and growth mechanism of vanadium carbonitrides in microalloyed steels, Scripta Materialia 187 (2020) 350–354, https://doi.org/10.1016/j.scriptamat.2020.06.041.

[95] P.G. Boswell, G.A. Chadwick, The formation and crystallization of an amorphous phase in an iron-carbon alloy, J Mater Sci 11 (1976) 2287–2296, https://doi.org/10.1007/BF00752093.

[96] P.H. Shingu, K. Shimomura, K. Kobayashi, R. Ozaki, An early stage of crystallization of amorphous Fe-C binary alloys obtained by splat cooling, Materials Science and Engineering 23 (1976) 183–186, https://doi.org/10.1016/0025-5416(76)90191-9.

[97] E. Bauer-Grosse, Thermal stability and crystallization studies of amorphous TM–C films, Thin Solid Films 447–448 (2004) 311–315, https://doi.org/10.1016/S0040-6090(03)01108-8.

[98] B. Lawrence, The production and crystallization of amorphous Fe-C alloys, University of British Columbia, 2017, https://doi.org/10.14288/1.0355248.

[99] G.R. Speich, Tempering of low-carbon martensite, Trans Met Soc AIME 245 (1969) 2553–2564.

[100] J. Wilde, A. Cerezo, G.D.W. Smith, Three-dimensional atomic-scale mapping of a cottrell atmosphere around a dislocation in iron, Scripta Materialia 43 (2000) 39–48, https://doi.org/10.1016/S1359-6462(00)00361-4.

[101] S.G. Wang, E.K. Tian, C.W. Lung, Surface energy of arbitrary crystal plane of bcc and fcc metals, Journal of Physics and Chemistry of Solids 61 (2000) 1295–1300, https://doi.org/10.1016/S0022-3697(99)00415-1.

[102] P. Błoński, A. Kiejna, Structural, electronic, and magnetic properties of bcc iron surfaces, Surface Science 601 (2007) 123–133, https://doi.org/10.1016/j.susc.2006.09.013.
[103] P.J. Dobson, B.J. Hopkins, Preferred orientation in metal films deposited on glass, Thin Solid Films 5 (1970) 97–103, https://doi.org/10.1016/0040-6090(70)90027-1.
[104] Carl.V. Thompson, R. Carel, Texture development in polycrystalline thin films, Materials Science and Engineering: B 32 (1995) 211–219, https://doi.org/10.1016/0921-5107(95)03011-5.
[105] J.J. Adams, D.S. Agosta, R.G. Leisure, H. Ledbetter, Elastic constants of monocrystal iron from 3 to 500 K, Journal of Applied Physics 100 (2006) 113530, https://doi.org/10.1063/1.2365714.
[106] T. Maeda, Y. Kawahara, K. Kinoshita, H. Sawada, J. Takahashi, R. Teranishi, K. Kaneko, An answer to the carbon cluster in low-temperature aged ferritic low-carbon steel, Materials Characterization 159 (2020) 110006, https://doi.org/10.1016/j.matchar.2019.110006.
[107] D. Kandaskalov, P. Maugis, Thermodynamic stabilities in the Fe-$Fe_{16}C_2$ system: Influence of carbon-carbon interactions studied by DFT, Computational Materials Science 150 (2018) 524–534, https://doi.org/10.1016/j.commatsci.2018.04.025.
[108] P. Zhang, S.X. Li, Z.F. Zhang, General relationship between strength and hardness, Materials Science and Engineering: A 529 (2011) 62–73, https://doi.org/10.1016/j.msea.2011.08.061.
[109] T. Tsuchiyama, K. Inoue, K. Hyodo, D. Akama, N. Nakada, S. Takaki, T. Koyano, Comparison of Microstructure and Hardness between High-carbon and High-nitrogen Martensites, ISIJ International 59 (2019) 161–168, https://doi.org/10.2355/isijinternational.ISIJINT-2018-404.
[110] Y.J. Li, A. Kostka, P. Choi, S. Goto, D. Ponge, R. Kirchheim, D. Raabe, Mechanisms of subgrain coarsening and its effect on the mechanical properties of carbon-supersaturated nanocrystalline hypereutectoid steel, Acta Materialia 84 (2015) 110–123, https://doi.org/10.1016/j.actamat.2014.10.027.
[111] A.H. Cottrell, B.A. Bilby, Dislocation Theory of Yielding and Strain Ageing of Iron, Proc. Phys. Soc. A 62 (1949) 49, https://doi.org/10.1088/0370-1298/62/1/308.
[112] K. Tapasa, Yu.N. Osetsky, D.J. Bacon, Computer simulation of interaction of an edge dislocation with a carbon interstitial in α-iron and effects on glide, Acta Materialia 55 (2007) 93–104, https://doi.org/10.1016/j.actamat.2006.08.015.
[113] Z. Xiong, I. Timokhina, E. Pereloma, Clustering, nano-scale precipitation and strengthening of steels, Progress in Materials Science 118 (2021) 100764, https://doi.org/10.1016/j.pmatsci.2020.100764.
[114] Y. Huang, S. Xu, X. Li, J. Gao, H. Zhao, S. Wang, T. Yang, S. Liu, X. Han, X. Mao, Cluster mediated high strength and large ductility in a strip casting micro-alloyed steel, Acta Materialia 276 (2024) 120102, https://doi.org/10.1016/j.actamat.2024.120102.
[115] H. Gleiter, Nanostructured materials: basic concepts and microstructure, Acta Materialia 48 (2000) 1–29, https://doi.org/10.1016/S1359-6454(99)00285-2.
[116] R. Rementeria, C. Capdevila, F.G. Caballero, Nanostructured Steels, in: R. Rana (Ed.), High-Performance Ferrous Alloys, Springer International Publishing, Cham, 2021, pp. 327–387, https://doi.org/10.1007/978-3-030-53825-5_8.